Aeroelastic Model for Design of Composite Propellers

Rotundo, C.D.; Sinnige, T.; Sodja, J.

DOI
10.2514/6.2024-2677

Publication date
2024

Document Version
Final published version

Published in
Proceedings of the AIAA SCITECH 2024 Forum

AIAA SciTech Forum
8-12 January 2024, Orlando, FL
AIAA SCITECH 2024 Forum

10.2514/6.2024-2677

Aeroelastic Model for Design of Composite Propellers

Carlo Rotundo *, Tomas Sinnige †, and Jurij Sodja ‡
Delft University of Technology, Delft, South Holland, 2629 HS, Netherlands.

A tightly coupled aeroelastic design code for composite propeller blades was developed, verified, and used to perform design sensitivity studies. The design code features a structural model that accounts for geometric nonlinearities through the application of a corotational framework, nonlinear responses to loads, and a cross-sectional modelling approach to accurately represent the detailed 3D blade structure as a reduced-order Timoshenko beam element model. Blade element momentum (BEM) theory was used to evaluate aerodynamic loads, which are mapped onto the structural mesh. The nonlinear aeroelastic analysis routine uses Newton's method to converge on a solution, with analytical derivatives for all applied loads. Excellent agreement with other analysis methods was shown during verification studies for all developed models. During validation, performance trends obtained from BEM were consistent with experimental results, with a maximum error of 20% at operating conditions under consideration during this research. The use of either symmetric-unbalanced or symmetric-balanced laminates was considered during sensitivity studies. Small variations in performance compared to the rigid propeller were observed from blades constructed out of symmetric-balanced laminates, as the minimal amount of bend-twist and extension-shear coupling resulted in small twist deformations. Conversely, propellers constructed out of symmetric-unbalanced laminates were shown to yield a noticeable variation in thrust and power compared to the rigid propeller due to the presence of bend-twist and extension-shear coupling, which results in coupling between twist and blade axis deformations. The presence of an aerodynamic wash-out effect was also found to alleviate blade loads, resulting in a lower power requirement at a given thrust setting, and an opposite trend was observed in the presence of a wash-in effect. The proposed analysis framework may be applied towards more extensive design studies or optimization in future projects.

Nomenclature

C_P	=	Power coefficient; $C_P = P/(\rho_\infty n^3 D^5)$
C_Q	=	Torque coefficient; $C_Q = Q/(\rho_\infty n^2 D^5)$
C_T	=	Thrust coefficient; $C_T = T/(\rho_\infty n^2 D^4)$
C_d	=	Sectional drag coefficient
C_l	=	Sectional lift coefficient
C_m	=	Sectional moment coefficient
C_q	=	Sectional torque coefficient
C_t	=	Sectional thrust coefficient
C_x	=	Sectional tangential force coefficient
C_z	=	Sectional axial force coefficient
D	=	Propeller diameter
J	=	Advance Ratio
$\boldsymbol{K_a}$	=	Aerodynamic stiffness matrix
$\boldsymbol{K_c}$	=	Centrifugal stiffness matrix
$\boldsymbol{K_e}$	=	Stiffness matrix for eccentric loads
$\boldsymbol{K_s}$	=	Structural stiffness matrix
$\boldsymbol{M}$	=	Mass matrix of beam element
P	=	Consumed Power
P_C	=	Power coefficient; $P_C = C_P\, J^{-3}$
Q	=	Propeller Torque
Q_C	=	Torque coefficient; $Q_C = C_Q\, J^{-2}$
$\underline{R}$	=	Residual vector of aeroelastic system
$\mathcal{S}_*$	=	Ply stacking sequence set (design study)
$\mathcal{S}_\mathrm{v}$	=	Ply stacking sequence set (verification)
T	=	Propeller Thrust
T_C	=	Thrust coefficient; $T_C = C_T\, J^{-2}$
V_eff	=	Resultant flow velocity at the blade section
V_∞	=	Resultant freestream flow velocity
a	=	Axial induction factor
a'	=	Azimuthal induction factor
c	=	Chord length
$\underline{f}_\mathrm{a}$	=	Aerodynamic load vector
$\underline{f}_\mathrm{c}$	=	Centrifugal force vector
$\underline{f}_\mathrm{e}$	=	Vector of externally applied loads
$\underline{f}_\mathrm{s}$	=	Internal structural load vector
n	=	Rotation rate of propeller (rev. / s)
$\underline{p}$	=	Structural degree of freedom deformations
q_∞	=	Dynamic pressure at propeller disk
r	=	Blade radial position
$\underline{r}$	=	Blade radial position in vector form
ΔS	=	Surface area of blade section
$\underline{\Omega}$	=	Vector form of rotation speed (rev. / s)
Θ	=	Ply orientation for sensitivity studies
α	=	Angle of attack of blade section
β	=	Twist angle of blade section
$\eta_\mathrm{e.h}$	=	Energy-harvesting efficiency; $\eta_\mathrm{e.h} = -8P_C/\pi$
η_P	=	Propeller efficiency; $\eta_\mathrm{P} = T_C/P_C = JC_T/C_P$
η_T	=	Turbine efficiency; $\eta_\mathrm{T} = P_C/T_C = C_P/(JC_T)$
φ	=	Incoming flow angle at the propeller disk
ρ_∞	=	Freestream air density

*MS Student, Faculty of Aerospace Engineering, Flight Performance and Propulsion, Kluyverweg 1, 2629 HS Delft, Member AIAA.
†Assistant Professor, Faculty of Aerospace Engineering, Flight Performance and Propulsion, Kluyverweg 1, 2629 HS Delft, Member AIAA.
‡Assistant Professor, Faculty of Aerospace Engineering, Aerospace Structures and Materials, Kluyverweg 1, 2629 HS Delft, Member AIAA.

I. Introduction

Recent interest in the development of hybrid- or fully electric propulsion systems has resulted from the imperative to mitigate greenhouse gas emissions within the rapidly expanding aerospace industry. This focus on electrified propulsion systems has prompted a resurgence in research towards the application of propeller-based propulsion systems. Furthermore, with batteries being used for energy storage and electric motors for supplying power, the electrification of aircraft enables the possibility for energy to be recovered during phases of flight where no power input is required.

Novel propeller design strategies are being explored to meet the growing demands for decreases in energy consumption and noise emissions of propeller-driven aircraft. One design approach that has been of interest recently is the application of aeroelastic tailoring towards the improvement of performance. Indeed, it has been shown by Dwyer and Rogers [1], Yamamoto and August [2], Khan [3, 4], Sandak and Rosen [5], Sodja *et al.* [6], and Möhren *et al.* [7], among others, that structural deformations of a propeller blade can noticeably affect aerodynamic performance at both on- and off-design conditions. In particular, coupling between bending and twisting deformations has been used to improve propeller performance through geometry modification in [5, 6] and through structural modifications in [3, 8, 9]. This effect can cause the propeller performance to either improve or deteriorate, depending on the operating conditions and the blade structural or geometric design. Moreover, Sandak and Rosen [5] and Sodja *et al.* [6] were successful in using bend-twist coupling to improve propeller performance at off-design conditions, as they showed that a blade with backward sweep and lean will deform favourably under load to broaden the range of advance ratio values corresponding to high-efficiency operation. Additionally, it was shown by Khan [3] that the introduction of bend-twist coupling can be used to satisfy several design objectives, such as to increase the thrust coefficient with constraints on deformations, or to increase efficiency with constraints on the thrust coefficient. These results indicate that the performance of a flexible propeller is sensitive to the presence of structural coupling, which may be exploited for improving performance. Thus, a composite propeller design and analysis framework has been developed during this research, to enable the inclusion of blade flexibility during the assessment of propeller performance. Computational efficiency and robustness have been prioritized during the development of this framework so that it may be used during optimization.

Static aeroelastic analysis procedures for flexible propellers have previously been developed or applied by other researchers, including Möhren *et al.* [7] and Gur and Rosen [10]. At the Delft University of Technology, an aeroelastic analysis framework, PROTEUS, was developed by Werter and De Breuker [11] and applied towards the conceptual design of aircraft wings in [12, 13] and wind turbine blades in [9, 14]. The structural model of PROTEUS is similar to the method applied in [7], as both models apply the finite-element method to solve deformations on a reduced-order Timoshenko finite element model, obtained from the 3D blade structure using a cross-sectional modeller. In PROTEUS, the cross-sectional modeller was developed by Ferede and Abdalla [15] and was shown to perform similarly to VABS (Variable Asymptotic Beam Section analysis), which is a commercial cross-sectional modelling program that was developed by Hodges [16]. During this research, the original version of PROTEUS (intended for the analysis of aircraft wings) has been modified to be applicable to propellers by implementing changes to the aerodynamic, structural, and aeroelastic models. The result of this work is an analysis routine with a medium-fidelity structural model and a low-fidelity aerodynamic model that may also be used during the optimization of composite dual-role propellers.

Another way of decreasing the overall energy consumption of propeller-driven aircraft is through the use of the propeller to generate energy during phases of flight where positive thrust is not required. In these cases, the propeller operates in its so-called *energy-harvesting mode*. Sinnige *et al.* [17] have shown that a propeller that is designed exclusively for propulsive operation will have a maximum energy harvesting efficiency of approximately 10% [17]. Conversely, Erzen *et al.* [18] saw a 19% decrease in energy consumption during the ascend/descend flight pattern and a 27% increase in the number of traffic pattern circuits performed with a dual-role propeller in comparison to a conventional propeller design when used during flight patterns that are conducive to regeneration during descent [18]. These results indicate that considering both positive-thrust and energy-harvesting mode during the design of propellers has the potential to yield at least a small decrease in energy consumption due to potential energy balance improvements that may be attained in descending flight, although poor performance during energy-harvesting mode should be expected.

Propellers that are designed for both positive-thrust and energy-harvesting conditions are called *dual-role propellers*, and may exhibit a compromise in performance between the two operating regimes because they are fundamentally opposite. Indeed, the design and operation of dual-role propellers involves considering two opposing load cases as shown in Fig. 1: positive thrust and torque during propulsive operation, and negative thrust and torque in energy-harvesting mode. This suggests that a propeller that is designed exclusively for propulsive operation will perform poorly in energy-harvesting conditions. Moreover, Sinnige *et al.* [17] have shown that a conventional propeller will exhibit a blade

loading distribution during energy-harvesting mode that does not resemble that of a typical minimum-induced-loss blade design. Several authors have shown that the decline in performance during energy-harvesting mode is largely due to the flow separation and associated viscous losses at the negative angles of attack at which the blade sections operate in this condition [19–21]. The application of aeroelastic tailoring towards the design of dual-role propellers may enable an improvement in performance at the two opposing operating conditions.

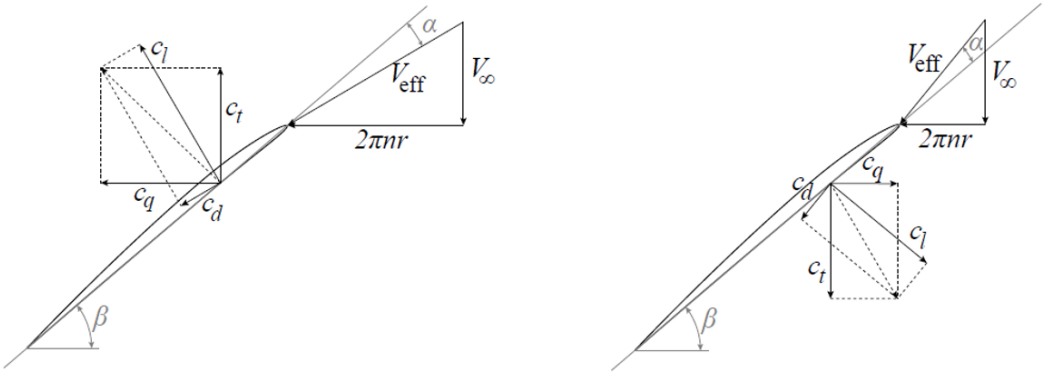

(a) propulsive mode.

(b) Energy-harvesting mode.

Fig. 1 Velocity triangles for a propeller operating in propulsive and energy-harvesting modes [17].

This research builds upon the work of Sodja *et al.* [6, 22], Khan *et al.* [3, 4], and Möhren *et al.* [7] through the introduction of a computationally efficient flexible composite propeller design framework, featuring a closely coupled aeroelastic analysis that is capable of accurately assessing performance during positive-thrust and energy-harvesting conditions. The analysis framework that was developed is capable of assessing the impact on performance of composite propeller blades constructed out of symmetric laminates. After completing the development and verification/validation of the aeroelastic analysis routine, sensitivity studies were performed both to demonstrate its capabilities and to provide preliminary structural design trends for propeller blades that are constructed out of symmetric-unbalanced or symmetric-balanced laminates. Lastly, due to its low computational cost, combined with its ability to evaluate any arbitrary blade geometric or structural design, the static aeroelastic design framework that was developed will be used in future projects towards optimization or more comprehensive design studies for composite propeller blades.

This paper is organized as follows: First, a summary of the propeller aeroelastic model that was developed is provided in Section II. Next, verification and validation of the developed models are provided in Section III. The proposed aeroelastic analysis routine was then used to perform design sensitivity studies, and the result of this investigation is presented in Section IV. A discussion on the main conclusions from this paper is then presented in Section V.

II. Propeller Analysis Overview

A schematic diagram of the analysis procedure that was developed is provided in Fig. 2, starting from the definition of inputs and ending at the post-processing of results. In the first step, the blade geometry and structural design data are read by the program. The geometry input is defined by spanwise airfoil coordinates, chord lengths, twist angles, leading edge locations, reference axis locations, and composite skin configurations. For each spanwise laminate of the structural design, eight lamination parameters and a constant thickness are defined. With the provided lamination parameters and thicknesses, the program calculates the structural properties of each laminate over the span of the blade. The analysis program then interpolates the geometric and structural information to spanwise locations defining the nodes of the structural mesh. Lastly, airfoil polar plots are generated, and aerodynamic coefficients are interpolated over the span of the blade before the analysis begins. After processing all the inputs and storing information on the operating conditions to be studied, the interpolated laminate properties and cross-sectional geometry are processed by the cross-sectional modeller to represent the structure as an equivalent finite element beam model. The static aeroelastic analysis is then performed, which couples a geometrically nonlinear Timoshenko beam model expressed using the co-rotational formulation to a BEM aerodynamic model. the results are post-processed after completing the analysis. For example, the cross-sectional modeller is used again to recover strains over the 3D geometry and performance trends are evaluated, as required during optimization to evaluate objectives and constraints. The structural, aerodynamic, and aeroelastic models are respectively discussed in more detail in Sections II.A, II.B, and II.C.

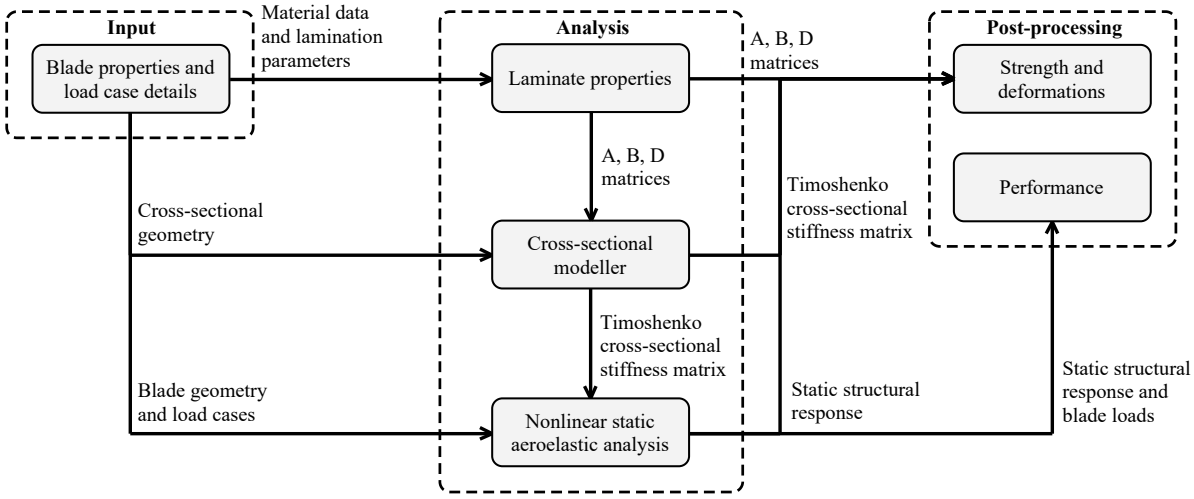

Fig. 2 A schematic representation of the static aeroelastic analysis routine.

A. Structural Model

The structural model that was used during this research is explained in detail by Werter [12], only the key aspects of this model are summarized in this section for brevity. The PROTEUS finite element model was extended to perform the structural analysis of composite propeller blades; this model receives inputs corresponding to the blade structural design (geometry, materials, laminate details) and outputs deformations, stresses, and strains. The properties of each laminate of the propeller blade are expressed in terms of lamination parameters, which are used to provide their corresponding $\{\boldsymbol{A}, \boldsymbol{B}, \boldsymbol{D}\}$ matrices according to classical laminated plate theory [23]. The cross-sectional modelling approach of Ferede [8] was used to calculate mass and stiffness matrices for the Timoshenko beam elements, as defined within the corotational framework that was formulated by Battini and Pacoste [24] and implemented by de Breuker [25] to account for geometric nonlinearities of the structure. The advantage of this approach is that it enables the blade structure to be equivalently represented using a significantly reduced number of degrees of freedom in comparison to the 3D model.

To enable the structural analysis to be suitable for propellers, the calculation of centrifugal forces and their derivatives must be added because the original implementation of PROTEUS was developed for aircraft wings. Centrifugal forces may be calculated using either the consistent or lumped mass matrix of each element, as shown in Eq. (1) and Eq. (2) The consistent mass matrix is used in cases that are not limited by computational cost, where greater precision is required, such as for individual analyses. The lumped mass matrix is used instead for cases that are limited by computational cost, where the decreased computational cost resulting from its use compensates for any losses in precision, such as during optimization. The derivative of centrifugal forces with respect to structural deformations, computed using Eq. (2), is required to solve the aeroelastic system of equations shown in Eq. (5):

$$\underline{f}_{\mathrm{c}} = -\boldsymbol{M} \cdot \left[\underline{\Omega} \times \left[\underline{\Omega} \times \left(\underline{r} + \underline{p}\right)\right]\right] = -\boldsymbol{M} \cdot \boldsymbol{\Omega} \cdot \boldsymbol{\Omega} \cdot \left(\underline{r} + \underline{p}\right) \tag{1}$$

$$\frac{\partial \underline{f}_{\mathrm{c}}}{\partial \underline{p}} = -\boldsymbol{M} \cdot \boldsymbol{\Omega} \cdot \boldsymbol{\Omega} = \boldsymbol{K}_{\mathbf{c}} \tag{2}$$

where $\boldsymbol{M}$ is either the consistent or lumped mass matrix, and $\boldsymbol{\Omega}$ is the skew-symmetric form of $\underline{\Omega}$.

B. Aerodynamic Model

The aerodynamic design and optimization of propellers has been under investigation for over a century, and a detailed history concerning the development of aerodynamic models for propellers has been provided by Wald [26]. It has been observed by Gur and Rosen [27] that blade element momentum (BEM) theory provides the best compromise between computational cost and precision in comparison to other aerodynamic modelling methods. For this reason, most aerodynamic analysis tools that are applied towards the conceptual design of propeller blades rely on BEM theory [26, 28]. The most notable open-source programs include CCBlade from Ning [29], QPROP and XROTOR from Drela [30], JavaProp from Hepperle [31], and JBLADE from Morgado [32–34]. In most cases, a variation of the theory of Adkins and Liebeck [35] is applied. A BEM code has accordingly been developed and applied during this project.

The advantage of using BEM to evaluate propeller aerodynamics is that it has a very low computational cost, whilst also being capable of accounting for all aerodynamic phenomena of interest to this study (i.e. root and tip losses, the stall-delay effect, and the turbulent wake state) when appropriate corrections are applied. With blade element momentum theory, the propeller blade aerodynamic loads are evaluated iteratively using both momentum theory and blade element theory, correcting the axial and tangential induced velocities until the loads evaluated with momentum theory are equal to the loads obtained from blade element theory. Thus, the 3D characteristic of the propeller flowfield is decomposed into a 1D conservation of momentum and 2D sectional aerodynamics. The BEM model that was developed is based on the theory of Adkins and Liebeck [35]. During analysis and optimization, propeller performance is evaluated using thrust (C_T and T_C), torque (C_Q and Q_C), and power (C_P and P_C) coefficients as well as efficiencies (η_P, η_T, and $\eta_\mathrm{e.h}$). The so-called energy harvesting efficiency, $\eta_\mathrm{e.h}$, is defined by Sinnige *et al.* [17] as the ratio between the power recovered by the propeller and the power available in the flow, and has a maximum theoretical value of 59.3% [36]. This metric is also used to assess the performance of wind turbines. In the context of wind turbine performance analyses, $\eta_\mathrm{e.h}$ is typically referred to as the power coefficient, P_C. Engineering correction models have been applied as follows:

- Root and tip losses have been corrected for using the well-known Prandtl tip loss factor [37]
- The rotational velocity of the propeller blade results in Coriolis and centrifugal forces that act on fluid particles in the boundary layer to delay the onset of separation to even higher angles of attack [38]. This has been accounted for using a modified version of XFOIL called RFOIL, which is documented by Bosschers *et al.* [39].
- At large negative axial induction factors (given by $a < -0.5$), axial momentum theory will return a negative velocity downstream of the propeller. This flow reversal is non-physical, as the actual flow entrains momentum from outside the wake [29]. The expression that was proposed by Burton *et al.* [40] is used to correct this. These conditions are unlikely to be encountered due to the low negative thrust settings that characterize energy-harvesting conditions, although this correction was applied to improve robustness of the proposed analysis method.

C. Aeroelastic Model

The primary objective of the aeroelastic analysis and optimization framework is to improve the conceptual design of composite propeller blades by including aeroelastic effects when evaluating performance. The resulting aeroelastic analysis is nonlinear, as nonlinear aerodynamic forces are permitted, and the structural model is capable of representing geometrical nonlinearities in addition to nonlinear structural responses to loads (such as the centrifugal stiffening effect). A schematic process-flow diagram of the nonlinear aeroelastic analysis procedure is shown in Fig. 3.

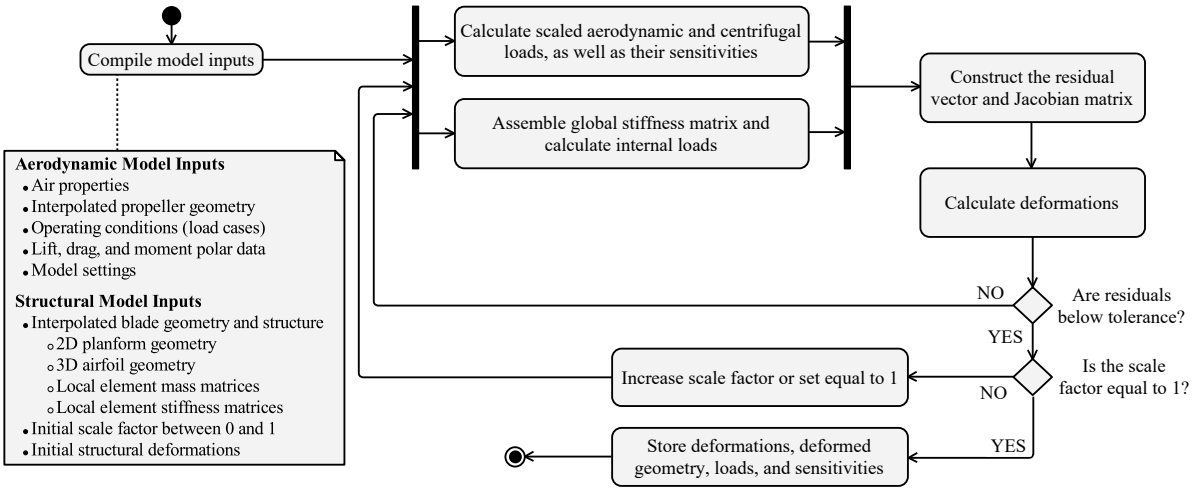

Fig. 3 A process-flow diagram indicating the nonlinear aeroelastic analysis procedure.

During the aeroelastic analysis, aerodynamic forces and moments are evaluated at the quarter-chord of each blade element. These loads are passed to the structural model, which projects the loads evaluated at each blade element onto the structural mesh. The aeroelastic analysis couples the aerodynamic and structural models using analytically calculated derivatives of each load vector in terms of the structural degrees of freedom. In this way, a tightly coupled aeroelastic model is established, which minimizes the residual function shown in Eq. (3). When the internal forces

are equal to the external forces, the residual function is exactly zero and energy is conserved at the fluid-structure interface. PROTEUS can also model constant external forces at eccentric nodes that are rigidly attached to the blade structure (denoted by $\underline{f}_e$). The eccentric forces either maintain a constant orientation or follow the blade's deformations. Externally applied eccentric forces were only required in Section III.A, $\underline{f}_e = \underline{0}$ for analyses shown in all other sections.

$$\underline{R}\left(\underline{p}\right) = \underbrace{\left[\underline{f}_s\left(\underline{p}\right)\right]}_{\text{internal}} - \underbrace{\left[\underline{f}_a\left(\underline{p}\right) + \underline{f}_c\left(\underline{p}\right) + \underline{f}_e\left(\underline{p}\right)\right]}_{\text{external}} \tag{3}$$

The external and internal forces encountered by the structure are purely dependent on structural deformations, as operating conditions and initial geometric parameters are otherwise fixed during the analysis. Eq. (3) is nonlinear, and a Newton-Raphson root finding algorithm is used to calculate deformations that minimize $\underline{R}$ in this work, as shown in Eq. (4) for the i^{th} iteration. In this way, the aeroelastic system of equations is provided in Eq. (5), where the derivative of each load vector is computed using analytical expressions.

$$\underline{R}\left(\underline{p}_{i+1}\right) \approx \underline{R}\left(\underline{p}_i\right) + \left[\frac{\partial \underline{R}}{\partial \underline{p}}\left(\underline{p}_i\right)\right] \cdot \left(\underline{p}_{i+1} - \underline{p}_i\right) := 0 \tag{4}$$

$$\implies -\underline{R}\left(\underline{p}_i\right) = \left[\frac{\partial \underline{f}_s}{\partial \underline{p}} - \frac{\partial \underline{f}_a}{\partial \underline{p}} - \frac{\partial \underline{f}_c}{\partial \underline{p}} - \frac{\partial \underline{f}_e}{\partial \underline{p}}\right]\Bigg|_{\underline{p}_i} \left(\underline{p}_{i+1} - \underline{p}_i\right) = \left[\boldsymbol{K_s} - \boldsymbol{K_a} - \boldsymbol{K_c} - \boldsymbol{K_e}\right]\left(\underline{p}_{i+1} - \underline{p}_i\right) \tag{5}$$

To stabilize the numerical solution process, a scale factor, λ_s, is applied as shown in Eq. (6) and gradually increased from zero to one. The nonlinear analysis proceeds as follows. First, the scale factor is initialized between zero and one, the residual function is then minimized for the system with scaled loads. After convergence is reached, the scale factor is increased and the residual function is minimized again. This process is repeated until convergence is reached with a scale factor that has a value of one, thus being equivalent to Eq. (5). Values for the scale factor and its step size were determined heuristically. Fast convergence was observed with an initial λ_s value of 0.5 and a step size of 0.5.

$$\left(\underline{f}_a\left(\underline{p}_i\right) + \underline{f}_c\left(\underline{p}_i\right)\right)\lambda_s - \underline{f}_s\left(\underline{p}_i\right) = \left[\frac{\partial \underline{f}_s}{\partial \underline{p}} - \left(\frac{\partial \underline{f}_a}{\partial \underline{p}} + \frac{\partial \underline{f}_c}{\partial \underline{p}}\right)\lambda_s\right]\Bigg|_{\underline{p}_i} \left(\underline{p}_{i+1} - \underline{p}_i\right) \tag{6}$$

As required to solve Eq. (5) and Eq. (6), derivatives of the aerodynamic loads were computed analytically according to Eq. (7). For the derivative calculation only, it has been assumed that static aerodynamic loads are only sensitive to twist deformations because deformations in the remaining five structural degrees of freedom yield relatively small changes in aerodynamic loads and the BEM model is insensitive to changes in sweep and lean. The full expression for the derivative of aerodynamic forces and moments with respect to twist deformations is shown in Eq. (8). The method that was applied to map derivatives from aerodynamic grid points to structural grid points is outlined in Appendix A.

$$\left(\frac{d}{d\underline{p}_a}\begin{bmatrix}\underline{\tilde{f}}_a \\ \underline{\tilde{m}}_a\end{bmatrix}\right) = \begin{bmatrix}\underline{0} & \underline{0} & \underline{0} & \underline{0} & \frac{d}{d\beta}\underline{\tilde{f}}_a & \underline{0} \\ \underline{0} & \underline{0} & \underline{0} & \underline{0} & \frac{d}{d\beta}\underline{\tilde{m}}_a & \underline{0}\end{bmatrix} \tag{7}$$

$$\begin{bmatrix}\frac{d\underline{\tilde{f}}_a}{d\beta} \\ \frac{d\underline{\tilde{m}}_a}{d\beta}\end{bmatrix} = q_\infty \Delta S \left(\begin{bmatrix}C_x & 0 & C_z & 0 & C_m c & 0\end{bmatrix}^T \left(\frac{2V_{\text{eff}}}{V_\infty^2}\right)\left(\frac{dV_{\text{eff}}}{d\beta}\right) + \begin{bmatrix}C_{x_\alpha} & 0 & C_{z_\alpha} & 0 & C_{m_\alpha} c & 0\end{bmatrix}^T \left(\frac{d\alpha}{d\beta}\right)\left(\frac{V_{\text{eff}}^2}{V_\infty^2}\right)\right) \tag{8}$$

After evaluating propeller performance using blade element momentum theory, the only unknown quantity contained within the first term of Eq. (8) is $dV_{\text{eff}}/d\beta$, which is computed using Eq. (9). Additionally, the only unknown quantities in Eq. (9) are the derivatives of the induction factors with respect to the pitch setting, $da/d\beta$ and $da'/d\beta$.

$$V_{\text{eff}} = \sqrt{\left(V_\infty\left(1+a\right)\right)^2 + \left(n\, r\left(1-a'\right)\right)^2} \implies \frac{dV_{\text{eff}}}{d\beta} = \frac{V_\infty^2\left(1+a\right)\frac{da}{d\beta} - \left(nr\right)^2\left(1-a'\right)\frac{da'}{d\beta}}{V_{\text{eff}}} \tag{9}$$

To evaluate the second term of Eq. (8), the normal and tangential force coefficients, C_z and C_x, are first differentiated with respect to α using Eq. (10). These derivatives depend on the angle of attack, Reynolds number, and Mach number.

$$\begin{bmatrix}C_{z_\alpha} \\ C_{x_\alpha}\end{bmatrix} = \begin{bmatrix}\cos\left(\varphi\right) & -\sin\left(\varphi\right) \\ \sin\left(\varphi\right) & \cos\left(\varphi\right)\end{bmatrix}\begin{bmatrix}C_{l_\alpha}\left(\alpha, Re, Ma\right) \\ C_{d_\alpha}\left(\alpha, Re, Ma\right)\end{bmatrix} \tag{10}$$

Derivatives of the lift, drag, and moment coefficients with respect to the angle of attack can be easily obtained numerically using polar data, and all aerodynamic performance quantities are already known from the BEM solution. Thus, the only term that is missing is the derivative of the angle of attack with respect to changes in twist angle, $d\alpha/d\beta$. An expression for this derivative is shown in Eq. (13) using the relationship between α, β, and φ.

$$\alpha = \beta - \varphi \implies \frac{d\alpha}{d\beta} = \frac{d\beta}{d\beta} - \frac{d\varphi}{d\beta} = 1 - \frac{d\varphi}{d\beta} \tag{11}$$

$$\frac{d\varphi}{d\beta} = \frac{d}{d\beta}\left(\arctan\left(\frac{V_\infty\,(1+a)}{n\,r\,(1-a')}\right)\right) = \frac{V_\infty\,n\,r\left(\frac{da}{d\beta}\,(1-a') + \frac{da'}{d\beta}\,(1+a)\right)}{(n\,r\,(1-a'))^2 + (V_\infty\,(1+a))^2} \tag{12}$$

$$\implies \frac{d\alpha}{d\beta} = 1 - \frac{V_\infty}{V_{\text{eff}}}\frac{n\,r}{V_{\text{eff}}}\left(\frac{da}{d\beta}\,(1-a') + \frac{da'}{d\beta}\,(1+a)\right) \tag{13}$$

With this derivation, all quantities are known except for the derivatives, $da/d\beta$ and $da'/d\beta$. Values for these terms are obtained through the use of an iterative process, according to the method presented in Appendix B.

III. Verification and Validation

Verification and validation of the proposed aeroelastic model is provided in this section. First, results verifying that the structural model is performing correctly are shown in Section III.A. Second, Section III.B contains results for the verification and validation of the aerodynamic analysis routine Verification of the complete aeroelastic analysis routine, including the analytical derivatives of aerodynamic loads with respect to changes in twist distribution, are provided in Section III.C. Validation of the structural and aeroelastic analysis routines has not been provided due to a lack of experimental data, it would be useful to provide validation for the aeroelastic analysis routine in a future project.

A. Structural Model Verification

To verify that the structural model was set up correctly, comparisons were made between the proposed model and a nonlinear ABAQUS finite element model. An aluminium cantilever box beam (60 mm height, 110 mm width, 1200 mm length, and 10 mm wall thickness) featuring centrifugal loads and a transverse distributed applied load of 5 N/mm over its full length was analysed, with results shown in Fig. 4. In ABAQUS, the structure was modelled using Timoshenko beam elements, and material properties used in ABAQUS and PROTEUS are shown in Appendix C. For the centrifugal force, a rotation rate of 100 RPS was applied, and the distributed load was set to follow the deformations of the beam so that it always acts orthogonally to the structural axis. The beam was also analysed without the centrifugal force. The maximum difference between the two sets of results is below 0.01%, thus verifying the proposed structural model.

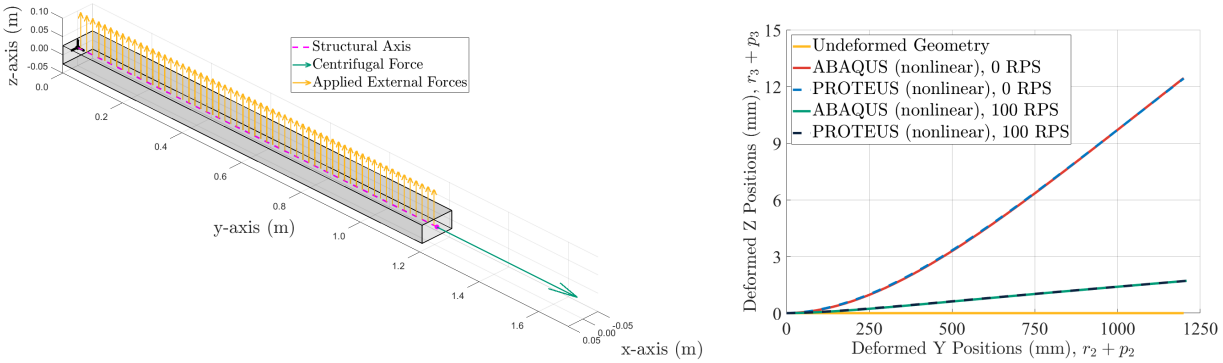

(a) Loads encountered by the beam

(b) Full beam deformations

Fig. 4 Results for the analysis of a beam model, providing verification for the structural analysis.

B. Aerodynamic Model Verification and Validation

The aerodynamic model has been validated through comparisons with the experimental results obtained by Nederlof *et al.* [20] for the 3-bladed version of the TUD-XPROP propeller (see Appendix C and [41] for details on the XPROP-3), and information on the experimental setup that was used to collect the data for comparison is provided in [20]. All results have been collected at sea-level for a fixed freestream velocity of V_∞ = 30 m/s. All BEM calculations were

performed using 50 cosine-spaced elements. Fig. 5 shows plots of the calculated power and thrust coefficient of the propeller at varying pitch angles, in comparison to the experimental results collected by Nederlof *et al.* [20] and the calculated results (using BEM with rotational effects included) from Goyal *et al.* [19]. Corresponding efficiency trends are subsequently plotted in Fig. 6 in comparison to the experimental results of Nederlof *et al.* [20].

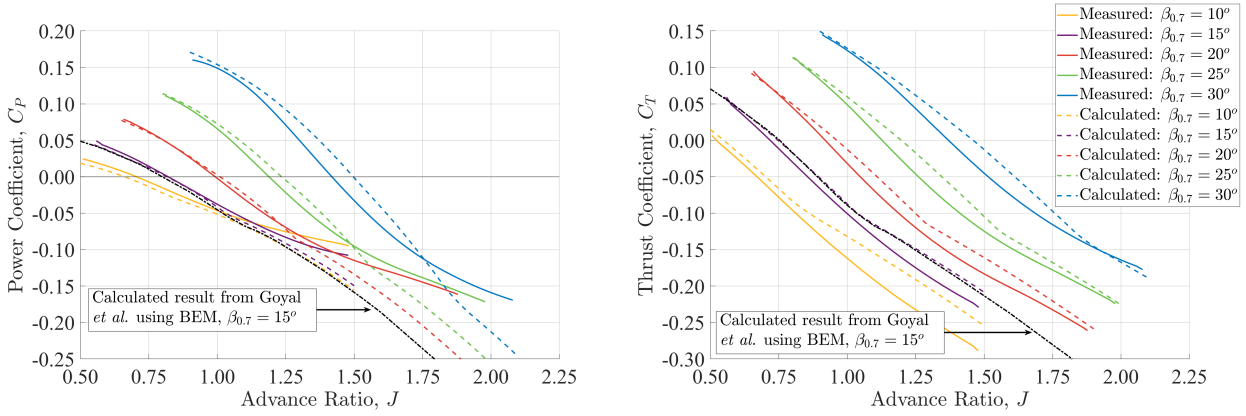

(a) C_P vs. J. (b) C_T vs. J.

Fig. 5 Plots of the calculated power and thrust coefficient for varying blade pitch settings in comparison to experimental results from Nederlof *et al.* [20] and calculated results from Goyal *et al.* [19].

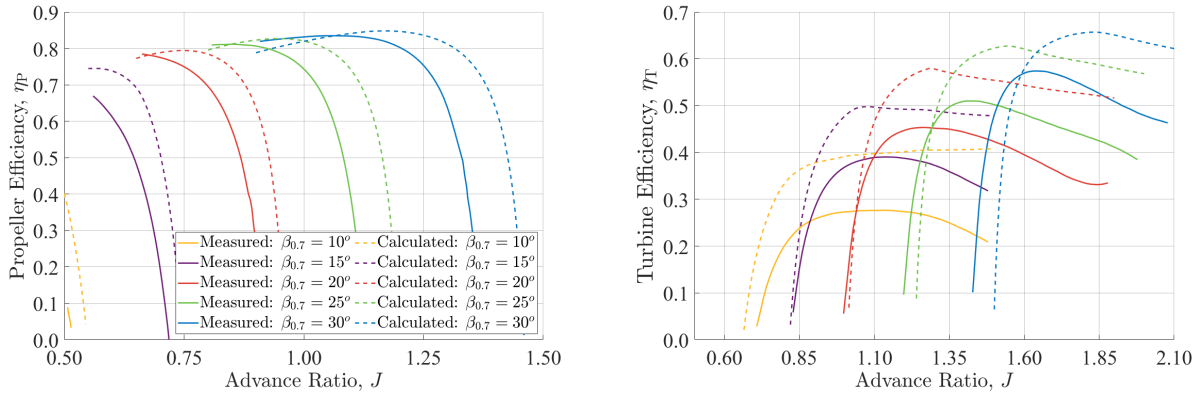

(a) η_P vs. J. (b) η_T vs. J.

Fig. 6 Calculated efficiency curves in comparison to experimental results from Nederlof *et al.* [20].

At all pitch settings that were considered, Fig. 5 indicates that the calculated power and thrust coefficients appear to exhibit the same trends as the experimental data at operating conditions corresponding to positive and low negative power coefficients. For an increasing negative thrust setting, corresponding to large advance ratio values, the BEM model tends to overpredict the amount of power that is recovered by the propeller. This is most likely caused by an incorrect prediction in the lift and drag coefficients at large negative angles of attack. These discrepancies grow as the amount of flow separation increases since RFOIL cannot accurately predict the lift and drag in regions with large amounts of separated flow, and generally can only provide an acceptable result for fully attached flows or flows with moderate amounts of separation [39]. Furthermore, in regions of separated flow, the assumption of zero aerodynamic interaction between neighbouring blade elements also becomes invalid [17]. Thus, the prediction of performance may be further improved by providing more accurate lift and drag polar input data at large negative angles of attack. This is currently not possible for the propeller model under consideration, as experimental data for the airfoils of the XPROP-3 do not exist. Although it is not possible to accurately predict performance at very high negative thrust settings, an acceptable range of advance ratio values may be considered for each pitch setting to limit the amount of blade loading, guaranteeing that the calculated C_T or C_P is not more than 20% greater than or less than the value obtained from physical tests. In Fig. 6, trends in both propeller and turbine efficiency are consistent between calculated and experimental results, although calculated efficiency curves are offset to the right of measured efficiency curves, indicating that the calculated

peak efficiency occurs at a higher advance ratio in comparison to the measured peak efficiency. The magnitude of this offset appears to grow with increasing pitch setting. This trend emerges primarily as a result of BEM overpredicting the thrust coefficient, and differences in the prediction of the power coefficient also contribute to this. This offset is not expected to have an effect on any of the conclusions that are reached during this research. Excellent agreement with the calculated results from Goyal *et al.* [19] has lastly been demonstrated, which shows that the BEM model is performing as expected despite its differences in comparison to the experimental results.

C. Aeroelastic Model Verification

Verification for the method that was applied to compute derivatives of aerodynamic loads is presented first in Section III.C.1, and verification for the complete aeroelastic analysis method is provided second in Section III.C.2.

1. Derivatives of Aerodynamic Loads

To verify that the method of evaluating derivatives of aerodynamic quantities from Section II.C was implemented correctly, results obtained using the proposed method were compared with results obtained from central differences, evaluated using Eq. (14):

$$\frac{dh}{d\beta}(\beta) \approx \frac{h(\beta+\Delta\beta) - h(\beta-\Delta\beta)}{2\Delta\beta} \tag{14}$$

where h is the aerodynamic quantity being differentiated and $\Delta\beta$ is the step size in twist angle.

To demonstrate differences observed between the sensitivities evaluated analytically and numerically, the unscaled TUD-XPROP-3 propeller (with geometry information provided in Appendix C) was analysed at a pitch setting of 20° over a range of advance ratio values between 0.6 and 1.5. Results for selected quantities, force and moment coefficients, as well as flow angles, are shown in Fig. 7. The absolute difference plots shown in Fig. 7 were calculated by taking the absolute value of the difference between derivatives from finite differences and from the proposed calculation.

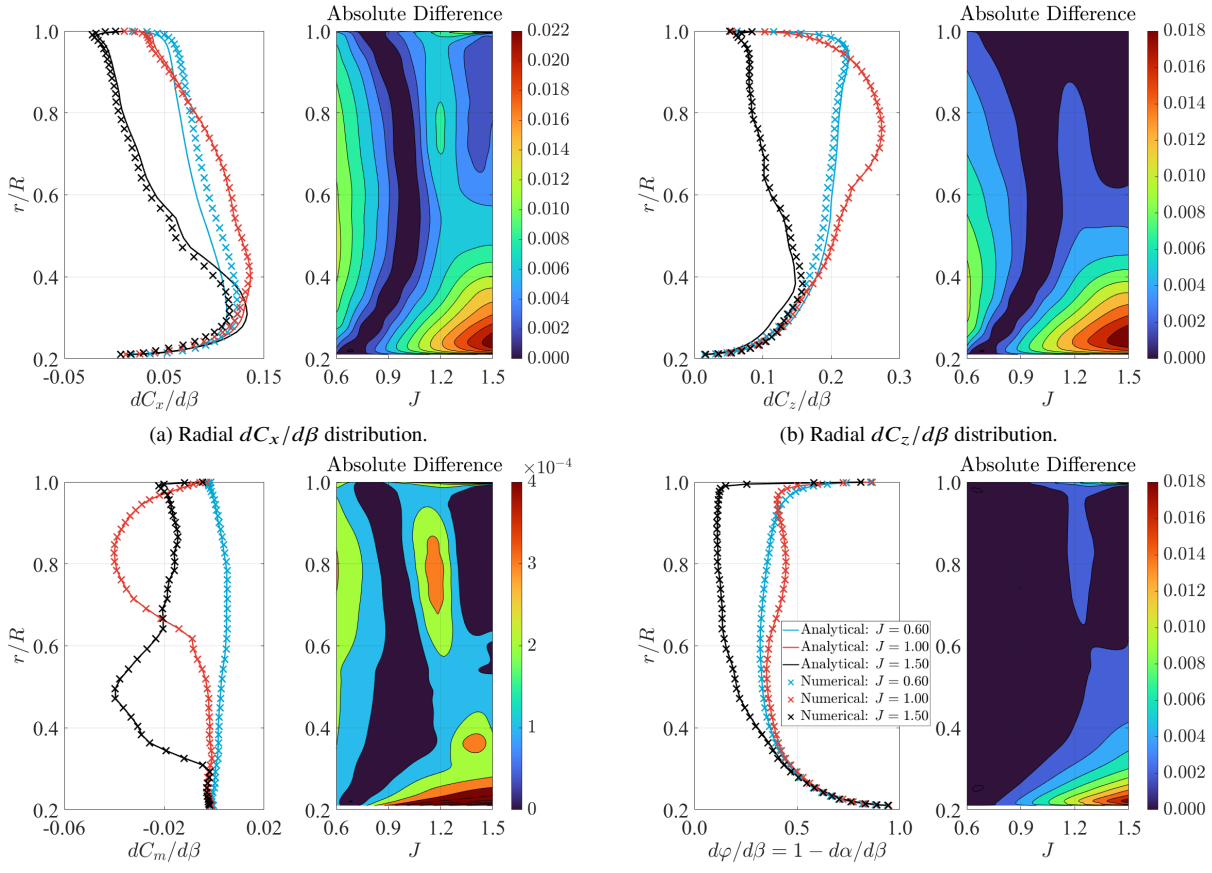

(a) Radial $dC_x/d\beta$ distribution.

(b) Radial $dC_z/d\beta$ distribution.

(c) Radial $dC_m/d\beta$ distribution.

(d) Radial $d\varphi/d\beta$ distribution.

Fig. 7 A comparison between derivatives computed numerically and analytically for the TUD-XPROP-3.

The step size used for the numerical calculation is given by $\Delta\beta = 10^{-4}$, whilst the step size for the lift and drag curve slopes used with the analytical calculation is given by $\Delta\alpha = 10^{-4}$. Values for the step sizes, $\Delta\beta$ and $\Delta\alpha$, were determined heuristically, as smaller step sizes were found to yield negligible differences in results that are obtained.

The results indicate that the quantities $dC_m/d\beta$ and $d\varphi/d\beta$ are nearly identical between the two methods. Near the root section, somewhat noticeable uncertainties are observed in results for the derivatives of the normal and tangential force coefficients, respectively $dC_z/d\beta$ and $dC_x/d\beta$. This also affects results obtained for derivatives of the dimensional forces, although these differences will not noticeably affect the overall performance or structural deformation due to the low dynamic pressure in this region, leading to small dimensional loads. The moment arm is also inherently small near the root section, which further suggests that uncertainties in this region will not have a noticeable effect on deformations. The derivative of the pitching moment coefficient is predicted with more precision than derivatives of the thrust and torque coefficients because it is not evaluated using an iterative method. The close agreement between the two methods lastly indicates that trends are predicted correctly using the proposed analytical approach, which verifies this method.

2. Aeroelastic Analysis

Due to a shortage of available experimental results to compare with during the validation of the aeroelastic analysis, verification was performed through comparisons to a loosely coupled method that proceeds by iteratively running the structural and aerodynamic analyses separately until the difference between deformations computed during two subsequent iterations is sufficiently small. This approach to providing validation for the aeroelastic analysis was considered sufficient because both the aerodynamic and structural models have already been validated, and thus the final remaining step is to demonstrate that the iterative scheme discussed in Section II.C is performing as intended. The loosely coupled method is very similar to the methods applied by Khan [3] and Sodja *et al.* [6], which do not require derivatives of aerodynamic forces with respect to structural degrees of freedom, and it proceeds as outlined below.

(1) Provide model inputs and initial conditions.
(2) Calculate aerodynamic and centrifugal loads.
(3) Apply loads to nodes of the structural mesh.
(4) Compute deformations using the finite element method.
(5) Modify the geometry input to the aerodynamic model (twist distribution and blade axis).
(6) If differences in deformations between subsequent iterations are above the defined tolerance, recompute aerodynamic loads. Otherwise, evaluate performance and end calculations.

A scaled version of the TUD-XPROP-3 was analysed, as shown in Fig. 8. Details on the structure and load cases that were considered are provided in Table 1. Ply angles are defined relative to the spanwise axis of the blade, positive towards the trailing edge for the upper and lower surfaces, and positive downwards for spar webs. Spar webs have been set as quasi-isotropic. The ply stacking sequence used for the upper and lower surfaces is shown in Eq. (15).

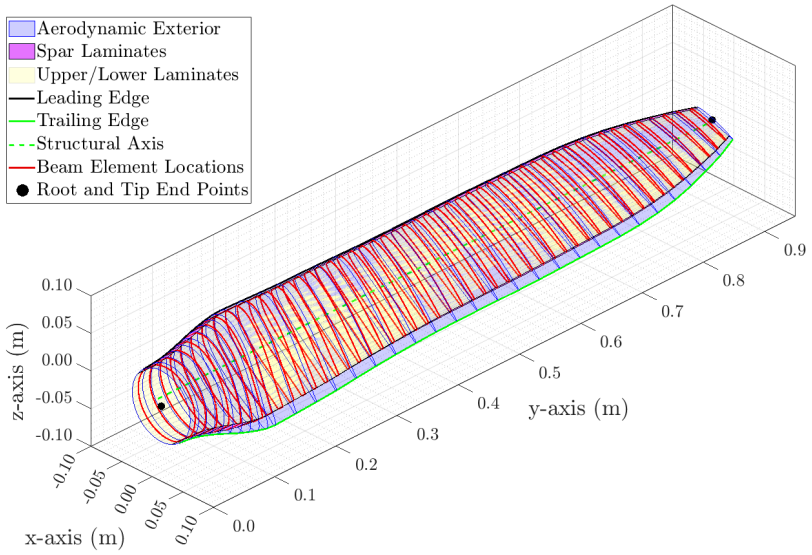

Fig. 8 A visual depiction of the blade geometry that was used during verification of the aeroelastic analysis.

$$\mathcal{S}_v = \left\{ \begin{array}{ccccccccc} 0^\circ & -15^\circ & -30^\circ & -30^\circ & -45^\circ & -45^\circ & -60^\circ & -60^\circ & -75^\circ & 90^\circ \end{array} \right\}_s \tag{15}$$

As shown above in Eq. (15), the ply stacking sequence that was selected for this case features only forward plies. This decision was made to ensure that a noticeable amount of bend-twist and extension-shear coupling is present, intending to introduce an aerodynamic wash-out effect. In this way, blade deformations will have a noticeable effect on performance and a correct solution can only be reached through the use of a nonlinear aeroelastic analysis. Front and rear spars were placed as near as possible to the leading and trailing edges whilst avoiding numerical difficulties, ensuring that the upper and lower surface skins are the primary load-carrying components of the structure. Moreover, each surface of the structure was parametrized with 1 spanwise laminate, meaning that 4 laminates of constant thickness were used to describe the blade. For the spacial discretization scheme, 75 linearly spaced beam elements were used for the structural analysis, 50 cosine spaced elements were used for the BEM model, and each structural cross-section was represented with 100 elements. Information on the propeller geometry and material properties considered during this study are provided in Appendix C. The blade dimensions were scaled up by a factor of 4.5 during this analysis to yield a blade of representative scale for application on a general aviation aircraft. Finally, a reference altitude of sea level was used for determining all required air properties, and the blade pitch setting was set to 25°.

Table 1 Structural information for the cases analysed to verify the aeroelastic model.

Case	Material	Geometry	Spars (%c)[a]	Laminate Thickness (mm)	Rotor Speed (RPS)	Advance Ratio
1	AS4 / APC2	TUD-XPROP-3	0.02, 0.90	0.75	40	0.75
2	AS4 / APC2	TUD-XPROP-3	0.02, 0.90	0.75	20	2.00

[a] Front and rear spars have been added because the cross-sectional modeller could not represent the stiffness properties of the leading and trailing edge sections. This change should not have any noticeable influence on general design trends.

As shown in Table 1, two cases were considered for this investigation. *Case 1* corresponds to operation in propulsive mode, and thus an advance ratio representing propulsive operation was selected. *Case 2* represents operation in energy-harvesting mode, and thus an advance ratio representing negative-power operation was selected. A higher rotor speed was used for case 1 in comparison to case 2 because the propeller will typically rotate slower in energy-harvesting mode in comparison to propulsive mode. A pitch setting of 25° was selected because comparisons with experimental data have been computed at this angle for the propeller under consideration (at a scale factor of 1.0), although any other realistic choice of pitch setting or rotor speed will yield the same level of agreement between the two considered analysis routines. Diagrams of the loading encountered by the blade in both the energy-harvesting and propulsive modes are shown in Fig. 9. For Fig. 9 only, loads have been scaled for visibility, and mapped onto the deformed blade geometry. The same scale factors have been used for the loads in both images, and thus it is possible to visually compare the magnitudes and directions of the loads between the two cases, although the numerical values do not have any physical meaning. The shapes of the force distributions and directions of the forces have thus been represented accurately.

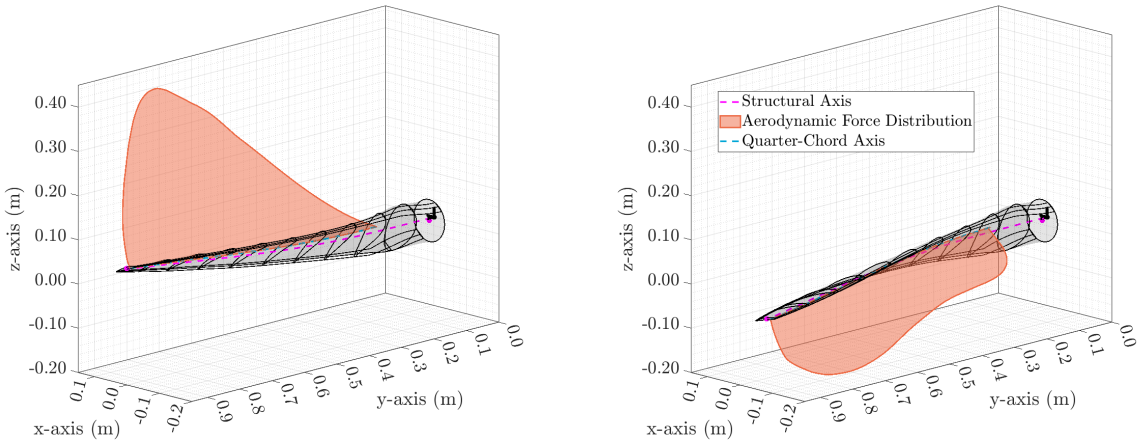

(a) Case 1 (propulsive operation)

(b) Case 2 (energy-harvesting operation)

Fig. 9 Blade models that were analysed to provide verification for the aeroelastic analysis.

In propulsive mode, the magnitude of the loads are greater than the magnitude of the loads in energy-harvesting mode. This is expected because a considerably higher thrust setting is being considered during propulsive mode in comparison to energy-harvesting mode. The blade also has a higher loading around its tip region in propulsive mode, whereas the load is more evenly distributed along the span of the blade in energy-harvesting conditions. Lastly, the loads act in opposite directions between the two operating conditions, as positive thrust and power characterize propulsive mode, whereas negative thrust and power characterize energy-harvesting mode.

Deformations and performance characteristics were compared between the loosely coupled and tightly coupled analysis methods. Translational and rotational degree of freedom deformations are plotted in Fig. 10, in the coordinates shown in Fig. 8. A very good level of agreement is demonstrated between deformation results obtained using the two analysis methods. Table 2 contains a summary of the overall propeller performance metrics for each case, including the percent difference between the results from each method. Excellent agreement was obtained between the two analysis methods, with a maximum difference that is below 0.01% for all quantities of interest. This level of agreement for both performance and deformation results verifies that the proposed analysis method is performing as expected. Three-dimensional plots of the blade deformations are additionally shown in Fig. 11 to indicate how deformations in each degree of freedom are represented on the three-dimensional structure. Lastly, plots of performance trends as a function of advance ratio are shown in Fig. 12, to demonstrate how the flexible propeller performs in comparison to the rigid propeller over a range of advance ratio values. Constant rotor speeds of 40 and 20 RPS were used respectively in positive and negative thrust conditions to maintain consistency with the two verification cases that were investigated.

Although there appears to be almost no difference between performance and deformation results obtained from the two analysis methods, the proposed tightly coupled method is more robust in comparison to the loosely coupled method, particularly for cases involving an aerodynamic wash-in effect, where structural deformations result in an increase in loading. To alleviate this concern, under-relaxation must be applied during the loosely coupled analysis, which results in a greater computational cost by at least an order of magnitude in comparison to the proposed tightly coupled method. The proposed tightly coupled method was found to converge on a solution in under 10 iterations.

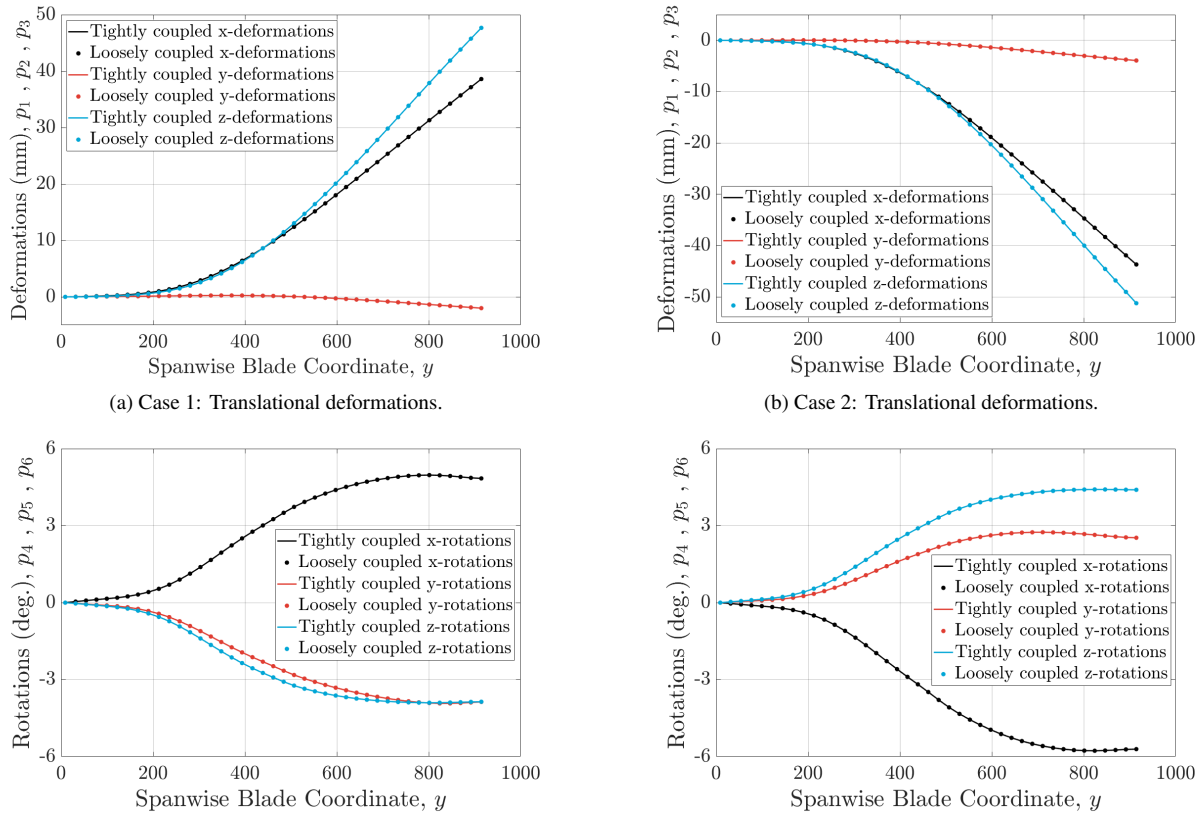

(a) Case 1: Translational deformations.

(b) Case 2: Translational deformations.

(c) Case 1: Rotational deformations.

(d) Case 2: Rotational deformations.

Fig. 10 Translational and rotational deformations obtained for the two cases under consideration.

Table 2 Performance results obtained for cases 1 and 2.

Case	Method	C_T	C_Q	C_P	η_P	η_T	$\eta_{e.h}$
1	Tightly Coupled	0.100	0.014	0.088	0.816	N/A	N/A
	Loosely Coupled (Percent Difference)	0.100 (0.001%)	0.014 (0.001%)	0.088 (0.001%)	0.816 (0.001%)	N/A	N/A
2	Tightly Coupled	-0.194	-0.048	-0.303	N/A	0.817	0.111
	Loosely Coupled (Percent Difference)	-0.194 (0.010%)	-0.048 (0.010%)	-0.303 (0.010%)	N/A	0.817 (0.010%)	0.111 (0.010%)

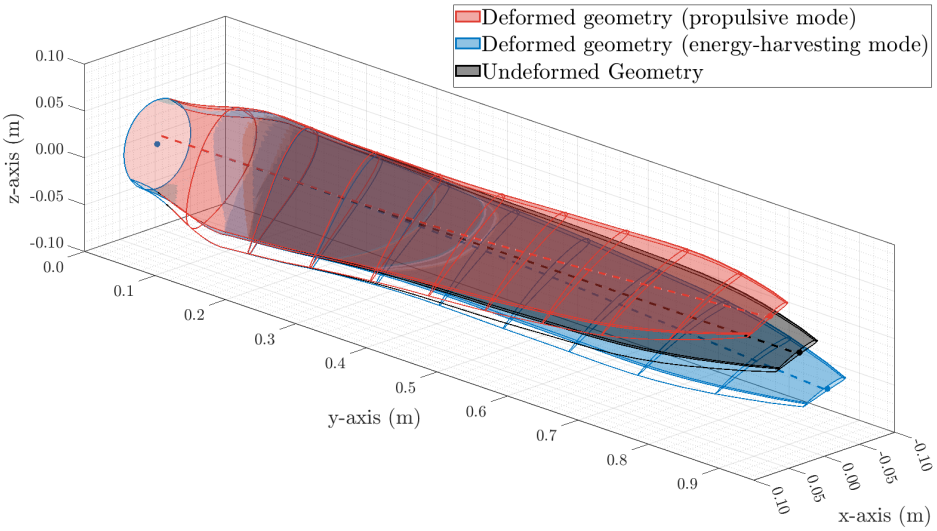

Fig. 11 Three-dimensional deformation plots obtained during verification studies.

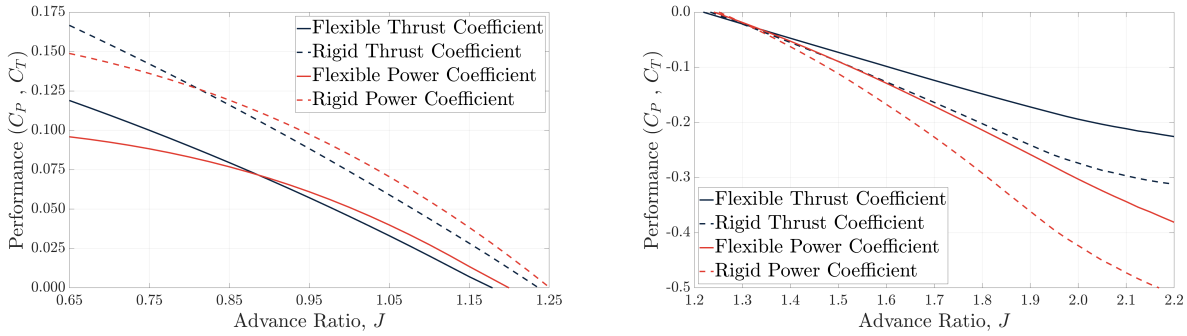

(a) Case 1 (propulsive operation), n = 40 RPS

(b) Case 2 (energy-harvesting operation), n = 20 RPS

Fig. 12 Plots of performance curves obtained during verification of the aeroelastic analysis.

With both the thrust and power coefficients of the flexible propeller showing decreased magnitudes in comparison to the rigid propeller in Fig. 12, an aerodynamic wash-out effect is clearly present in both propulsive and energy-harvesting conditions. The presence of an aerodynamic wash-out effect is also made clear in Fig. 10c and Fig. 10d, as torsional deformations that reduce the twist angle are shown in propulsive mode and torsional deformations that increase the twist angle are shown in energy-harvesting mode. These deformations result in a reduced angle of attack in both cases. This is expected, as only negative ply orientations were used on both the upper and lower surfaces of the blade.

IV. Design Sensitivity Study Results

Design sensitivity studies are presented in this section to provide insights regarding structural design trends and physical mechanisms affecting variations in propeller performance. In particular, the use of symmetric-unbalanced laminates has been compared with the use of symmetric-balanced laminates to define the propeller blade structure, highlighting performance and deformation trends that are obtained with each laminate type over a range of ply orientations. The results shown in this section lastly demonstrate some capabilities of the proposed analysis routine.

A. Design Study Setup

To maintain commonality, the propeller blade geometry that was used during the verification study of the complete aeroelastic analysis in Section III.C.2 was again used for the sensitivity studies shown in this section, including the same pitch setting, scale factor, material, spar web locations, and spatial discretization scheme. Thus, the blade pictured in Fig. 8 again describes the blade geometry that was used during this investigation. The only difference between the blade from Section III.C.2 and the blade that was used for the sensitivity studies is that the laminate thickness of all surfaces of the blade was doubled from a value of 0.75 millimetres to a value of 1.50 millimetres in this case. The decision to change the laminate thickness was made to ensure that the maximum tip displacement does not exceed a value of 5% of the tip radius, which improves the feasibility of the structural design. Ultimately, a compromise was made between feasibility and sensitivity to changes in ply orientation, as a thinner laminate will yield larger variations in performance and the primary objective of the design sensitivity studies is to provide insights into how changes in ply orientation affect deformations and performance. The chosen laminate thickness was therefore considered to be the largest value to yield variations in performance and deformations with ply orientation that are sufficient for comparison.

The propeller blade was defined with one laminate each for its upper and lower surfaces, as well as for each of its spar webs. The same laminate was always used for the upper and lower surfaces, and a constant quasi-isotropic laminate was always used to define the two spar webs. For the upper and lower surfaces, two laminate types were considered during this work: symmetric-unbalanced and symmetric-balanced. The ply stacking sequence defining symmetric-unbalanced laminates is given by Eq. (16), and Eq. (17) defines the ply stacking sequence for symmetric-balanced laminates. For any ply angle, given by $\Theta \in \{-90^\circ, -75^\circ, \ldots, +90^\circ\}$, the stacking sequence of the upper surface laminate is equivalent to the stacking sequence of the lower surface laminate. For symmetric-unbalanced laminates, changing the ply orientation directly changes the major principal stiffness axis, as it will always align with the angle Θ. Conversely, symmetric-balanced laminates will have two major stiffness directions, mainly aligned with $\pm\Theta$. As a result of the constant plies with orientations of 90° and 0°, the major principal stiffness axis for symmetric-balanced laminates will either have an angle of approximately 0° or 90°, depending on which angle $|\Theta|$ is closest to, and at $\Theta = \pm 45^\circ$, the maximum stiffness will be equally distributed between angles of +45° and −45°. Thus, the presence of constant ply angles of 0° and 90° potentially reduces the amount of bend-twist coupling from symmetric-balanced laminates, although the decision to include these angles was made to improve the feasibility of the structural design, and the resulting decrease in bend-twist coupling is not expected to have any effect on the main conclusions from this investigation. Supplementary plots of the stiffness rosettes are provided in Appendix D to support the discussion on the direction of the primary stiffness axis. For all ply stacking sequences used for laminates considered during the design sensitivity studies, ply angles are defined relative to the spanwise axis of the blade, positive towards the trailing edge.

Symmetric-Unbalanced:
$$\mathcal{S}_* = \left\{ 90^\circ \quad 0^\circ \quad \vdots \quad \Theta \quad \Theta \quad \Theta \quad \Theta \quad \Theta \quad \Theta \quad \vdots \quad 0^\circ \quad 90^\circ \right\}_s \tag{16}$$

Symmetric-Balanced:
$$\mathcal{S}_* = \left\{ 90^\circ \quad 0^\circ \quad \vdots \quad \Theta \quad -\Theta \quad \Theta \quad -\Theta \quad \Theta \quad -\Theta \quad \vdots \quad 0^\circ \quad 90^\circ \right\}_s \tag{17}$$

B. Results

Performance trends are shown in Section IV.B.1 and deformation trends are shown in Section IV.B.2. For comparisons between symmetric-balanced and symmetric-unbalanced laminates, results were collected over a range of advance ratio values at each ply orientation under consideration, while holding the rotor speed constant at a value of $\Omega = 23$ RPS to maintain a constant centrifugal force, effectively reducing some bias from the results. In this way, the advance ratio was varied between values of 0.35 and 1.70 by directly varying the freestream velocity only.

1. Performance Trends

Plots of the thrust and power coefficient are shown in Fig. 13 for both symmetric-unbalanced and symmetric-balanced laminates. For symmetric-unbalanced laminates, Fig. 13a and Fig. 13c indicate that ply orientations yielding a decrease

in thrust coefficient will also cause the power coefficient to decrease. This was found to occur for negative ply orientations, which generally induce an aerodynamic wash-out effect as the blade deforms, causing upward displacements to result in leading-edge-down pitch rotations that reduce the loading. For symmetric-unbalanced laminates with positive ply orientations, an aerodynamic wash-in effect is observed as the blade deforms, which conversely causes upwards displacements to yield leading-edge-up pitch deformations that increase the loading. Fig. 13b and Fig. 13d indicate that variations in performance for symmetric-balanced laminates are significantly smaller in comparison to performance variations for symmetric-unbalanced laminates. This low sensitivity to changes in ply orientation for symmetric-balanced laminates is caused by the absence of extension-shear coupling and the negligible bend-twist coupling.

For symmetric-unbalanced laminates, the largest decrease in thrust and power appears to be present at ply orientations between $-30°$ and $-15°$. Conversely, the largest increase in thrust and power appears to be present at ply orientations between $+15°$ and $+30°$. This is consistent with the observation that changes in performance are closely linked to the presence of bend-twist and extension-shear coupling, as a large amount of extension-shear and bend-twist coupling is present between these angles. For symmetric-balanced laminates, it appears that the performance trends approximately overlap for ply orientations of $\pm 90°$ and $0°$, $\pm 75°$ and $\pm 15°$, as well as $\pm 60°$ and $\pm 30°$. The laminates corresponding to each pair are the same, except offset from each other by $90°$. Thus, they have the same amount of torsional and shear stiffness. Because the aerodynamic loads exert a leading-edge-down pitching moment on the blade, which increases with advance ratio (this will be explained in more detail in the discussion of the deformation trends associated with Fig. 16b), the loading encountered by the flexible propeller without any coupling is always decreased relative to the rigid propeller, and this difference in loading grows with increasing aerodynamic loads.

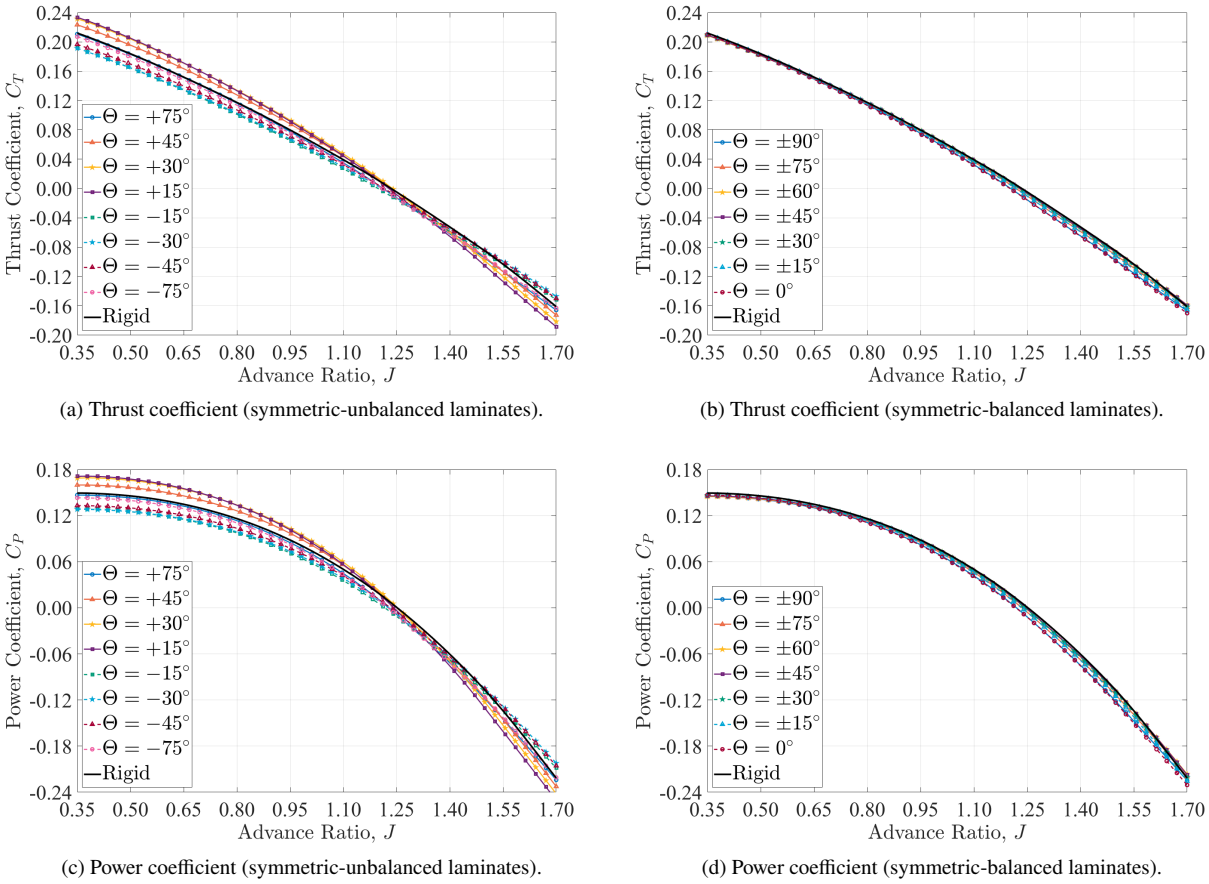

(a) Thrust coefficient (symmetric-unbalanced laminates).

(b) Thrust coefficient (symmetric-balanced laminates).

(c) Power coefficient (symmetric-unbalanced laminates).

(d) Power coefficient (symmetric-balanced laminates).

Fig. 13 Plots of thrust and power coefficients as a function of the advance ratio.

The most important conclusion to draw from the results presented in Fig. 13 is that the difference in performance is largely dependent on pitch deformations of the propeller, and thus aeroelastic tailoring may only be used to enhance performance through the inclusion of extension-shear or bend-twist coupling. As a result, symmetric-balanced laminates provide a minimal change in performance because they provide a negligible amount of bend-twist and

extension-shear coupling. On the other hand, symmetric-unbalanced laminates have the potential to provide a substantial amount of bend-twist and extension-shear coupling, and thus may yield a significant change in thrust and power that can either enhance or degrade performance, depending on the type of coupling that is present. The application of symmetric-unbalanced laminates towards the improvement of performance should therefore be explored further.

To clarify trends in performance that are shown in Fig. 13, the thrust and power coefficients have been plotted as a function of the ply orientation at constant advance ratio values in Fig. 14. The thrust and power coefficient difference terms that are plotted on the vertical axis of Fig. 14 are computed using Eq. (18):

$$\left.\begin{aligned} \Delta C_T &= C_T^{\text{flexible}} - C_T^{\text{rigid}} \\ \Delta C_P &= C_P^{\text{flexible}} - C_P^{\text{rigid}} \end{aligned}\right\} \tag{18}$$

where coefficients with the superscript "flexible" correspond to results obtained with the flexible propeller and coefficients with the superscript "rigid" correspond to results obtained with the rigid propeller. The difference in thrust and power coefficients have been plotted in Fig. 14 instead of the actual thrust and power coefficient values to enable the effect on performance resulting from variations in ply orientation at each fixed advance ratio to be easily compared.

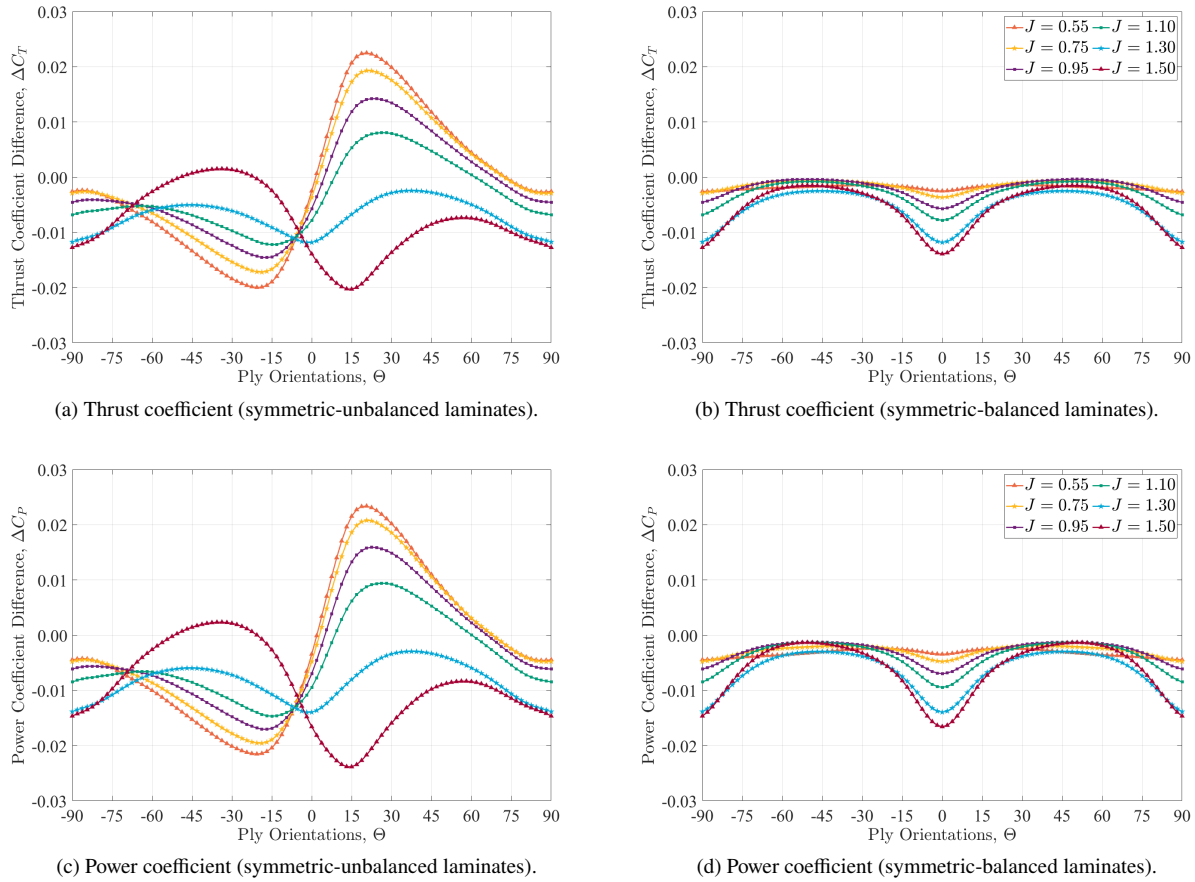

(a) Thrust coefficient (symmetric-unbalanced laminates).

(b) Thrust coefficient (symmetric-balanced laminates).

(c) Power coefficient (symmetric-unbalanced laminates).

(d) Power coefficient (symmetric-balanced laminates).

Fig. 14 Plots of thrust and power coefficients as a function of the ply orientation.

Symmetric-unbalanced laminates exhibit noticeable variations in performance, whereas symmetric-balanced laminates have already been shown to yield small variations in performance, and this trend is confirmed again in Fig. 14. It is clear from Fig. 14b and Fig. 14d that variations in performance for symmetric-balanced laminates are dependent primarily on the amount of torsional and shear stiffness that the blade has, as variations are smallest for ply orientations of ±45°, where the shear and torsional stiffness are largest, and variations in performance grow as ply orientations approach 0° or ±90°. Symmetric-balanced laminates always appear to yield lower thrust and power coefficients in comparison to the rigid baseline case due to the leading-edge-down aerodynamic pitching moment that is generated by the blade, which results in a natural aerodynamic wash-out effect during propulsive mode and a wash-in effect during

energy-harvesting mode. On the other hand, the main takeaway from Fig. 14a and Fig. 14c is that symmetric-unbalanced laminates with negative ply orientations yield an aerodynamic wash-out effect that tends to alleviate loads, resulting in a decrease in magnitude for both the thrust and power coefficients, whereas positive ply orientations yield an aerodynamic wash-in effect that causes thrust and power coefficient magnitudes to increase. For symmetric-unbalanced laminates, the torsional and shear stiffness of the laminate has a secondary effect on performance, whilst the presence of bend-twist and extension-shear coupling has the most substantial effect on performance, as the largest variations in performance occur for angles given by $15^\circ \leq |\Theta| \leq 30^\circ$, which correspond to the most amount of structural coupling.

Efficiency plots are lastly shown in Fig. 15 for both balanced and unbalanced laminates to indicate the laminate configurations that are beneficial or detrimental to overall performance. The trends in efficiency vs. advance ratio are less clear than the trends in thrust and power. This is because the differences in blade loading for each ply orientation at a constant advance ratio will affect the relative magnitudes of the deformations, which will ultimately influence performance. Thus, it is difficult to make a direct comparison in the efficiency trends yielded by each ply orientation when plotted against advance ratio. These plots have still nevertheless been shown for completeness.

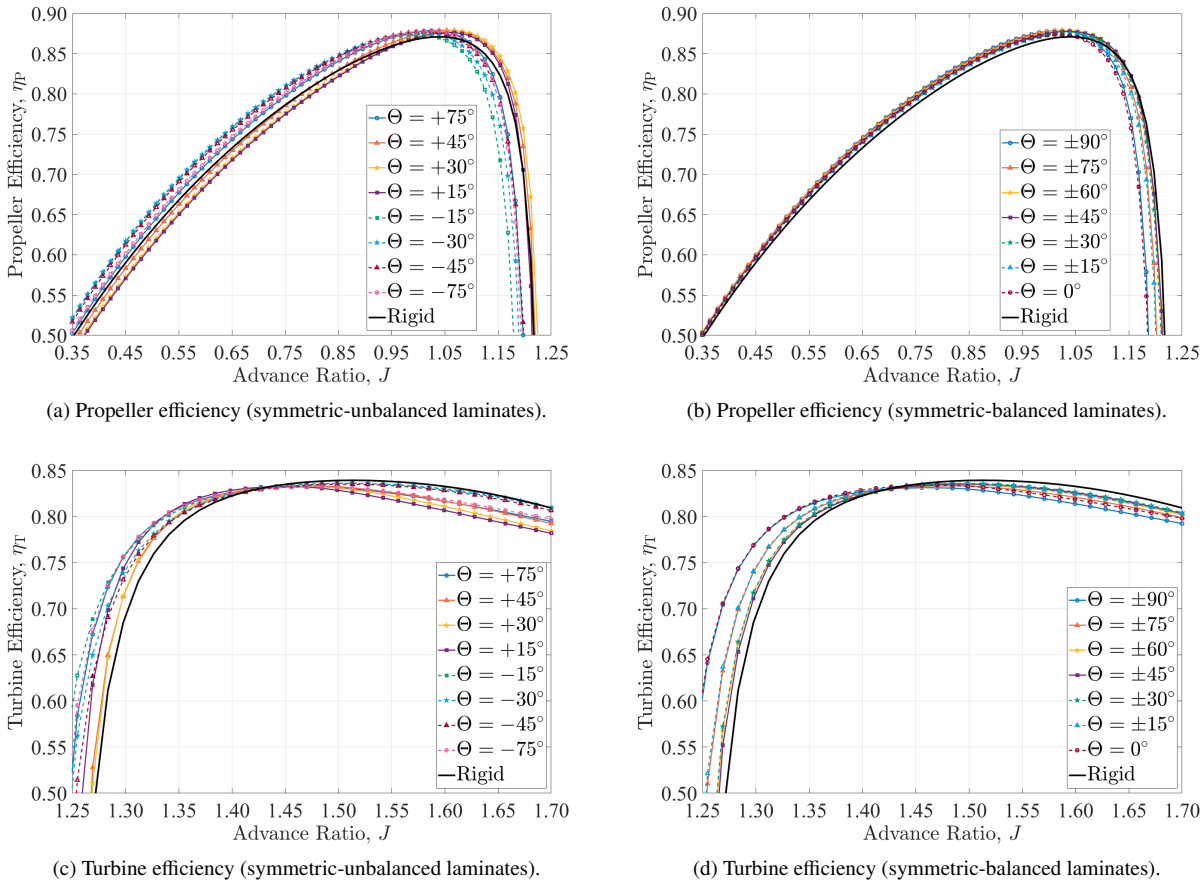

(a) Propeller efficiency (symmetric-unbalanced laminates).

(b) Propeller efficiency (symmetric-balanced laminates).

(c) Turbine efficiency (symmetric-unbalanced laminates).

(d) Turbine efficiency (symmetric-balanced laminates).

Fig. 15 Propeller and turbine efficiency plots as a function of the advance ratio.

The propeller efficiency appears to either be increased or decreased depending on the ply orientations, although the turbine efficiency appears to always decrease through the consideration of blade flexibility. For symmetric-unbalanced laminates, Fig. 15a indicates that negative ply orientations result in a larger propeller efficiency in comparison to the rigid propeller, whereas positive ply orientations yield a lower propeller efficiency in comparison to the rigid propeller. All flexible propellers yield a similar peak propeller efficiency value that always appears to exceed the peak value of the rigid propeller. It is also shown in Fig. 15c that the turbine efficiency is always lower or close to equivalent for the flexible propeller in comparison to the rigid propeller, although ply orientations between approximately -30° and -15° appear to exhibit the greatest turbine and propeller efficiency. Ply orientations between approximately $+15^\circ$ and $+30^\circ$ conversely exhibit the lowest propeller and turbine efficiency. These trends emerge as a result of the type of structural coupling that is present, which is elaborated on in Section IV.B.2. For symmetric-balanced laminates, Fig. 15d indicates

that the flexible propeller always underperforms in comparison to the rigid propeller, with the best turbine efficiency being demonstrated for ply orientations of ±45°, which exhibits performance trends that are closest to that of the rigid propeller. Differences in performance for symmetric-balanced laminates are primarily driven by the amount of torsional and shear stiffness that is associated with each ply orientation, as discussed further in Section IV.B.2.

2. *Deformation Trends*

The first set of deformation results presented are plots of twist deformations around the y-axis as a function of the advance ratio, as shown in Fig. 16. These results are most interesting because they precisely indicate the presence and type of structural coupling, as the aerodynamic loads provide a relatively small pitching moment contribution. These results also show the pitch deformation tendencies of the blade in the absence of any coupling.

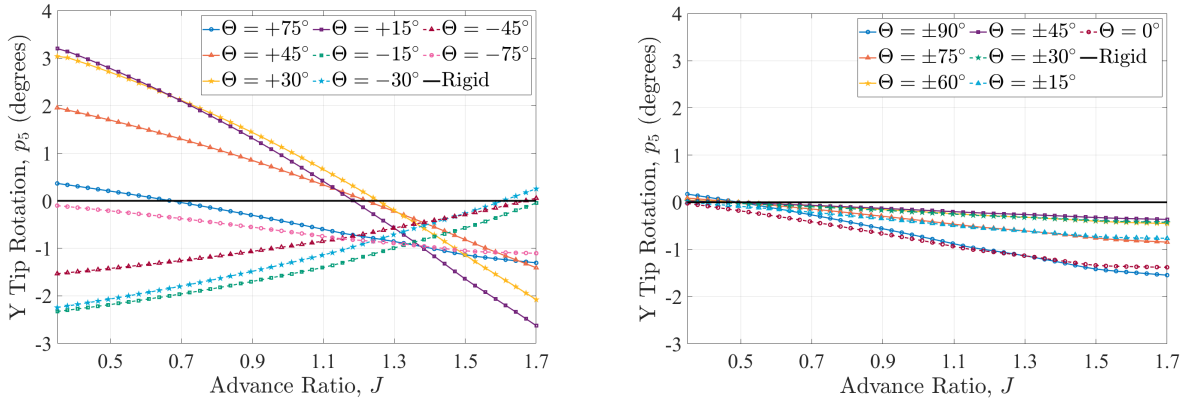

(a) Symmetric-unbalanced laminates.

(b) Symmetric-balanced laminates.

Fig. 16 Plots of blade tip torsional deformations as a function of the advance ratio.

For symmetric-unbalanced laminates, the significant differences in pitch deformations are primarily caused by the presence of extension-shear and bend-twist coupling. This is indicated by the significant differences observed between symmetric-balanced and symmetric-unbalanced laminates. The negative slope of pitch angle deformations with increasing advance ratio for symmetric-unbalanced laminates with positive ply orientations shown in Fig. 16a indicates a wash-in effect. This is consistent with the results shown in Fig. 13a, which indicated positive ply orientations to yield more thrust and power at a constant advance ratio in comparison to negative ply orientations of the same absolute angle value. For laminates with negative ply orientations, the opposite type of coupling exists, as indicated by the positive slope with respect to advance ratio, due to the presence of a wash-out effect. For laminates with ply orientations of equivalent values and opposite signs, the positive ply orientations have a slope with a slightly greater magnitude in comparison to the negative ply orientations due to the aerodynamic pitching moment, which tends to increase in the leading-edge-up direction with increasing thrust. Thus, using positive ply orientations yields a similar structural response to the forward-swept blade that was studied by Sodja *et al.* [6], whereas negative ply orientations yield a similar structural response to the backward-swept blade that was investigated by Sodja *et al.* [6]. Lastly, the most amount of coupling was found at ply angles near ±15° and ±30°, which is made clear by the slope of the pitch rotation vs. advance ratio curve shown in Fig. 16a being of the largest magnitude at these angles. The largest variations in performance were also identified near these angles in Fig. 13a, Fig. 13c, Fig. 14a, Fig. 14c, Fig. 15a, and Fig. 15c.

For symmetric-balanced laminates, Fig. 16b indicates that the propeller blade structure encounters a natural aerodynamic wash-out effect as a result of the leading-edge-down pitching moment that is generated by the blade at almost all advance ratios that were considered. This wash-out effect decreases in strength as the advance ratio decreases (and thus as the aerodynamic forces increase) because the structural axis is aft of the quarter-chord line. Ply orientations of ±45° have the most amount of torsional stiffness, and the torsional stiffness decreases as plies become more closely aligned. As a result, the least amount of pitch deformations and variations in performance are observed at angles of ±45°. Moreover, the magnitude of torsional deformations increases as ply orientations approach 0° and 90°. The torsional stiffness is equivalent for laminates with ply orientations of 0° and ±90°, ±15° and ±75°, and ±30° and ±60°, as each pair of angles corresponds to equivalent laminates that are offset from each other by an angle of 90°. An analogous trend in performance has also been observed, with the largest variation in performance being encountered at ply orientations

corresponding to the least amount of shear and torsional stiffness. In comparison to their counterparts, laminates with smaller angles in each pair have more stiffness in bending due to the majority of their plies being more closely aligned with the blade axis, and thus their pitch deformation vs. advance ratio curves shown in Fig. 16b have a decreased slope.

Plots of signed net tip displacements as a function of the advance ratio are shown in Fig. 17 to indicate how varying the primary stiffness axis affects bending deformations. Positive displacements correspond to operation in propulsive conditions, and negative displacements correspond to operation in energy-harvesting conditions. The main conclusions from the tip displacement plots shown in Fig. 17 are that the stiffness increases as the ply orientations become more closely aligned with the blade axis, and because the loading is negligibly affected by the ply orientation for symmetric-balanced laminates, the deformation magnitude is equivalent for laminates with orientations of either $(+\Theta, -\Theta)$ or $(-\Theta, +\Theta)$. On the other hand, the presence of bend-twist coupling, which results in either an aerodynamic wash-in or wash-out effect, will affect the amount of loading that the blade constructed out of symmetric-unbalanced laminates experiences. Thus, symmetric-unbalanced laminates with positive ply orientations will encounter larger deformations than symmetric-unbalanced laminates with negative ply orientations of the same angle.

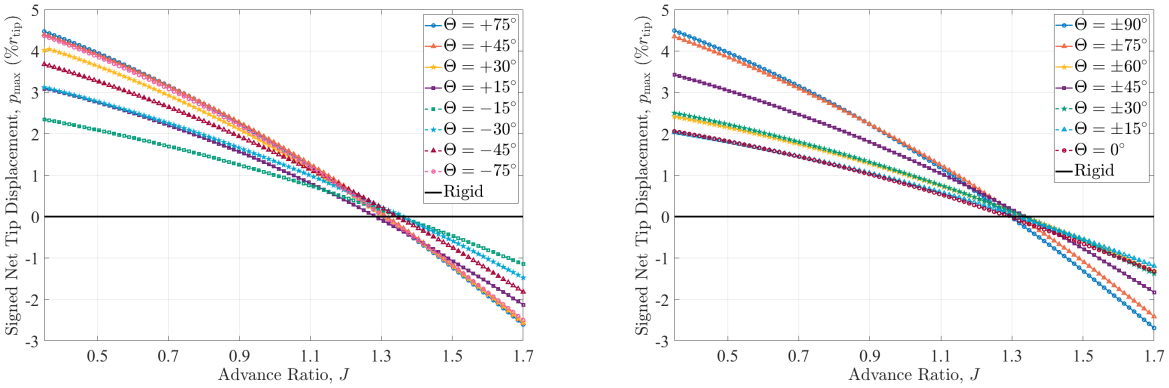

(a) Symmetric-unbalanced laminates.

(b) Symmetric-balanced laminates.

Fig. 17 Signed blade tip displacement plots as a function of advance ratio, with $p_{max} = \pm\sqrt{p_1^2 + p_2^2 + p_3^2}$.

In the plots of tip displacement vs. thrust, the more consistent loading makes it somewhat easier to observe the trend in magnitude with changing ply orientation. This is especially true for symmetric-balanced laminates, where it has been shown in Fig. 13 that the thrust and power coefficients are quite similar between each ply orientation, indicating a similar amount of loading at each constant advance ratio. For symmetric-unbalanced laminates, Fig. 13 instead shows a much larger difference in thrust and power coefficient, which suggests more considerable differences in the amount of loading encountered at different ply orientations for a constant advance ratio. Lastly, it is interesting to observe that propellers with symmetric-unbalanced laminates that have ply orientations between $-30°$ and $-15°$ exhibit the lowest tip displacement magnitudes, as shown in Fig. 17a, in addition to the best performance, as shown in Fig. 15a and Fig. 15c. This result demonstrates the potential for aeroelastic tailoring to be applied towards the design of propeller blades.

The final plots shown correspond to torsional deformations and signed net tip displacements as a function of the ply orientation for several constant advance ratios, shown in Fig. 18. The most noticeable result from these plots is that trends in pitch deformations are analogous to trends in variations in performance, shown in Fig. 14, and the physical reasoning behind the trends in pitch deformations shown in Fig. 18a and Fig. 18b follows directly from the discussion concerning Fig. 14. This similarity between pitch deformations and performance variations occurs because variations in performance are driven primarily by pitch deformations. Although the BEM model that was used during this research is insensitive to changes in blade axis geometry (with exception to radial deformations, which generally have a negligible influence on performance), it is still likely that pitch deformations have the largest effect on variations in performance. Nevertheless, a physical model of the propeller would likely exhibit variations in performance due to changes in blade sweep and lean as well, and these effects could not be captured during this investigation. The tip displacement plots, shown in Fig. 18c and Fig. 18d, indicate that tip displacement magnitudes are primarily affected by the stiffness of the laminate, whereas pitch deformations are governed almost entirely by the presence of bend-twist or extension-shear coupling. Indeed, the tip displacements consistently increase as ply orientations approach $\pm 90°$, where the stiffness under the loads encountered by the blade is lowest. The tip displacement accordingly decreases as plies become aligned

with the blade axis. Moreover, the presence of bend-twist and extension-shear coupling appears to provide a clear influence on the tip displacements obtained with symmetric-unbalanced laminates in Fig. 18c. Mainly, negative ply angles exhibit a load alleviation effect, which reduces deformations, and positive ply angles have the opposite effect. Nevertheless, the majority of displacements are caused directly by the transverse and centrifugal forces that the blade encounters and thus deformations are influenced most by the amount of bending stiffness that the blade has. This suggests that coupling may be used to enhance the blade's performance whilst still reducing its tip displacements.

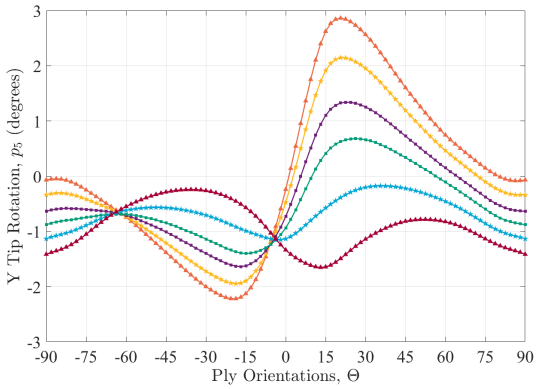

(a) Torsional deformations (symmetric-unbalanced laminates).

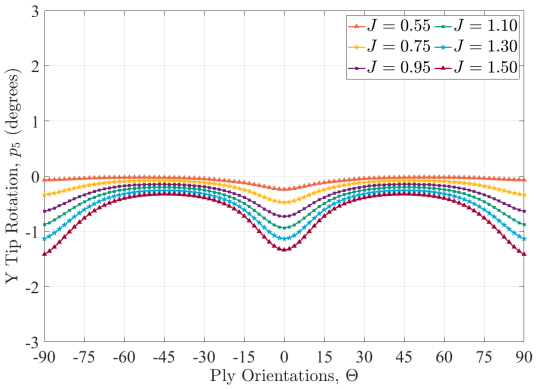

(b) Torsional deformations (symmetric-balanced laminates).

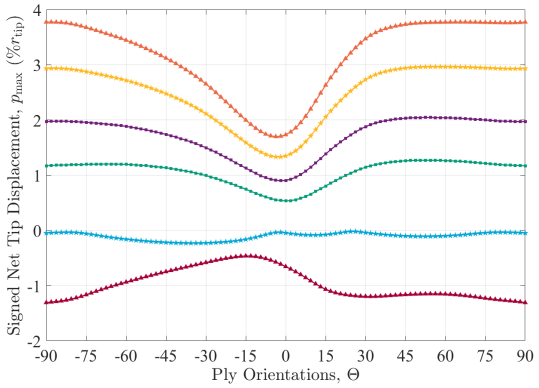

(c) Signed net tip displacement (symmetric-unbalanced laminates).

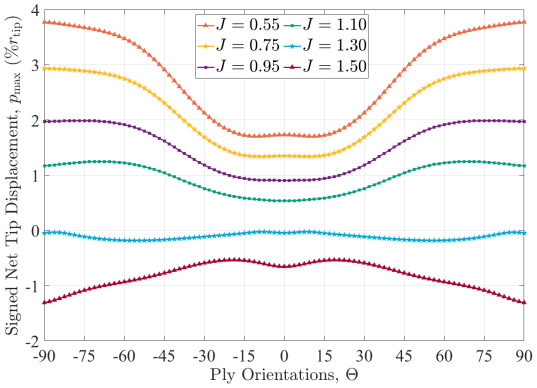

(d) Signed net tip displacement (symmetric-balanced laminates).

Fig. 18 Blade tip deformation plots as a function of the ply orientation.

V. Conclusions

A tightly coupled aeroelastic analysis routine was proposed, featuring an aerodynamic model that is based on blade element momentum theory and a structural model that is capable of handling geometrical nonlinearities and nonlinear loads. The aerodynamic model was validated through comparisons with experimental data, which showed agreement with general trends and a maximum uncertainty that is below 20% at all operating conditions that would be of interest during a design study. Very good agreement was observed during verification studies, when comparing results obtained with the proposed model with results from an existing BEM code. Verification studies were also completed for both the structural and aeroelastic models, resulting in an excellent agreement with the selected reference cases, for which a maximum error of less than 0.01% was obtained. The aeroelastic analysis framework that was developed and verified is capable of modelling detailed composite blade geometries with an arbitrary number of laminates distributed along its spanwise and chordwise axes. Due to its low-fidelity aerodynamic model, combined with its medium-fidelity structural model, the analysis routine has a low computational cost, which makes it suitable for use in an optimization routine.

After verifying that the proposed aeroelastic analysis procedure was properly implemented, design sensitivity studies were conducted using the TUD-XPROP-3 propeller, enlarged by a factor of 4.5 to yield a blade of a representative scale for application on a general aviation aircraft. Through the application of aeroelastic tailoring, both a wash-in and a wash-out aeroelastic response of the blade may be achieved using symmetric and unbalanced laminates. With

laminates that are symmetric and balanced, variations in performance between the flexible and rigid propellers were less apparent due to the absence of extension-shear coupling and the small amount of bend-twist coupling. As expected, the presence of an aerodynamic wash-out effect tended to improve performance through the alleviation of loads, whereas the presence of a wash-in effect tended to degrade performance though the augmentation of loads. It was interestingly shown that introducing an aerodynamic wash-out effect can improve the efficiency in both propulsive and energy-harvesting conditions, whilst suppressing bending deformations. The proposed aeroelastic analysis framework will be applied in future investigations towards more comprehensive design sensitivity analyses and optimization studies.

Acknowledgements

Jatinder Goyal, cited as Goyal *et al.* [19], provided the baseline BEM code that was used during development and verification of the aerodynamic model, in addition to polar plots from RFOIL for the TUD-XPROP, as required for all aerodynamic analyses. Robert Nederlof, cited as Nederlof *et al.* [20], provided the experimental data that was used during validation of the aerodynamic model.

A. Mapping Loads and Derivatives between Eccentric Nodes and Structural Grid Points

If an applied external force or moment is located at one of the structural nodes, then it is relatively straightforward to include it within the analysis. However, in most cases, applied loads are eccentric, and thus must be appropriately handled by the finite-element solver, such that equivalent loads are applied at the structural degrees of freedom instead. The calculation of eccentric forces and their sensitivities is based on the work of de Breuker [25] and Werter [12], who applied the formulation developed by Battini and Pacoste [24] to allow for both constant and follower eccentric forces and moments. For completeness, a discussion on the formulation used to define eccentric loads and their derivatives has been provided within this section, although further details may be found within references [12, 24, 25]. This derivation has been repeated in this work because it is essential for the calculation of sensitivities for the aerodynamic forces, as they always act at points that are eccentric to the structural nodes.

For any structural element, eccentric forces can be applied at any location, at a distance of $\underline{v}_0$ from the line that joins the two end nodes of the element. Considering nodes k and $k+1$ of the structure, which have position vectors given by $\underline{x}_k$ and $\underline{x}_{k+1}$, an input eccentric force and moment can be applied at a location of $\underline{x}_\mathrm{a} + \underline{v}_0$, where $\underline{x}_\mathrm{a}$ is a point on the element that joins $\underline{x}_k$ and $\underline{x}_{k+1}$. The normalized distance between $\underline{x}_\mathrm{a}$ and $\underline{x}_k$ is given by ξ, which is defined as follows.

$$\xi = \frac{||\underline{x}_\mathrm{a} - \underline{x}_k||}{||\underline{x}_{k+1} - \underline{x}_k||} \implies 1 - \xi = \frac{||\underline{x}_{k+1} - \underline{x}_\mathrm{a}||}{||\underline{x}_{k+1} - \underline{x}_k||}$$

Diagrams of this scenario are provided in Fig. 19 for clarity.

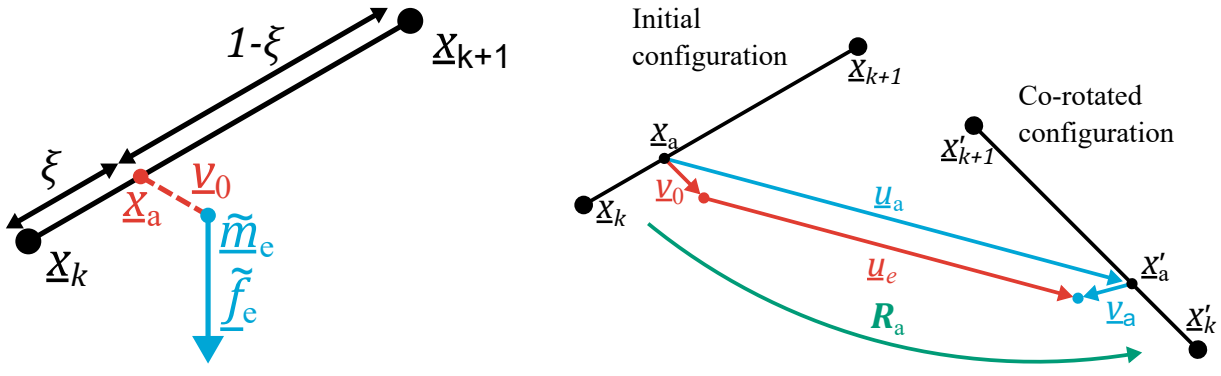

(a) The eccentric force applied to the undeformed structure.

(b) A diagram of the displacement of eccentric forces.

Fig. 19 Schematic diagrams of the eccentric forces and moments (adapted from [12]).

The location of the applied force in the initial configuration is given by $\underline{x}_\mathrm{e}$ in Eq. (19), shown below, where $\underline{v}_0$ is defined as a rigid link that is orthogonal to the beam element, as depicted in Fig. 19a.

$$\underline{x}_\mathrm{e} = \underline{x}_\mathrm{a} + \underline{v}_0 \tag{19}$$

Fig. 19b indicates that the rigid link may be converted into its corotated orientation as follows:

$$\underline{v}_a = \boldsymbol{\mathcal{R}}_{\mathbf{a}} \cdot \underline{v}_0 \tag{20}$$

where $\boldsymbol{\mathcal{R}}_{\mathbf{a}}$ is the rotation matrix that converts rigid links from the undeformed configuration to the corotated configuration.

Using Fig. 19, displacements of the location of the applied load are related to displacements of the nearest point on the beam element, $\underline{x}_a$, as shown below.

$$\underline{u}_a + \underline{v}_a = \underline{v}_0 + \underline{u}_e \tag{21}$$

$$\implies \underline{u}_e = \underline{u}_a + [\boldsymbol{\mathcal{R}}_{\mathbf{a}} - \boldsymbol{I}_{\mathbf{3x3}}] \cdot \underline{v}_0 \tag{22}$$

To transfer the applied load acting at $\underline{x}_e$ onto the two nodes of the beam element, Eq. (23) ensures that the virtual work of the equivalent loads acting at the two nodes must be equal to the virtual work of the eccentric load:

$$\delta \underline{p}_e^T \begin{bmatrix} \underline{\tilde{f}}_e \\ \underline{\tilde{m}}_e \end{bmatrix} = \begin{bmatrix} \delta \underline{p}_k^T & \delta \underline{p}_{k+1}^T \end{bmatrix} \begin{bmatrix} \underline{f}_k \\ \underline{m}_k \\ \underline{f}_{k+1} \\ \underline{m}_{k+1} \end{bmatrix} \qquad \underline{p} = \begin{bmatrix} \underline{u} \\ \underline{\theta} \end{bmatrix} \tag{23}$$

where the total rotational pseudo-vector of the eccentric point is given by $\underline{\theta}_e$, the total rotational pseudo-vectors of the two end nodes are given by $\underline{\theta}_k$ and $\underline{\theta}_{k+1}$, and displacement vectors of the two nodes are denoted by $\underline{u}_k$ and $\underline{u}_{k+1}$. Forces and moments are denoted respectively by $\underline{f}$ and $\underline{m}$, with subscripts to denote whether they apply to nodes k or $k+1$.

Using the relations derived above and the assumption of equivalent virtual work, Werter [12] derived a relationship between deformations of the eccentric node and global deformations of the two end nodes of the beam element in variational form, where $\underline{\vartheta}_a$ is the spatial angular variation at the eccentric node.

$$\delta \underline{u}_e = \delta \underline{u}_a + \delta \boldsymbol{\mathcal{R}}_{\mathbf{a}} \underline{v}_0 \tag{24}$$

$$\delta \boldsymbol{\mathcal{R}}_{\mathbf{a}} = \delta \boldsymbol{\vartheta}_{\mathbf{a}} \boldsymbol{\mathcal{R}}_{\mathbf{a}} \tag{25}$$

$$\implies \delta \underline{u}_e = \delta \underline{u}_a + \delta \boldsymbol{\vartheta}_{\mathbf{a}} \boldsymbol{\mathcal{R}}_{\mathbf{a}} \underline{v}_0 = \delta \underline{u}_a + \delta \boldsymbol{\vartheta}_{\mathbf{a}} \underline{v}_a = \delta \underline{u}_a - \boldsymbol{v}_{\mathbf{a}} \delta \underline{\vartheta}_a \tag{26}$$

$$\implies \delta \underline{p}_e = \begin{bmatrix} \delta \underline{u}_e \\ \delta \underline{\theta}_e \end{bmatrix} = \begin{bmatrix} (1-\xi)\, \boldsymbol{I}_{\mathbf{3x3}} & -(1-\xi)\, \boldsymbol{v}_{\mathbf{a}} & \xi \boldsymbol{I}_{\mathbf{3x3}} & -\xi \boldsymbol{v}_{\mathbf{a}} \\ \boldsymbol{0}_{\mathbf{3x3}} & (1-\xi)\, \boldsymbol{I}_{\mathbf{3x3}} & \boldsymbol{0}_{\mathbf{3x3}} & \xi \boldsymbol{I}_{\mathbf{3x3}} \end{bmatrix} \begin{bmatrix} \delta \underline{u}_k \\ \delta \underline{\vartheta}_k \\ \delta \underline{u}_{k+1} \\ \delta \underline{\vartheta}_{k+1} \end{bmatrix} = \boldsymbol{B}_{\mathbf{e}} \cdot \begin{bmatrix} \delta \underline{p}_k^g \\ \delta \underline{p}_{k+1}^g \end{bmatrix} \tag{27}$$

To transform the spatial angular variation into the variation of the total rotational pseudo-vector, the relation that was derived by Ibrahimbegovic [42] has been applied as follows.

$$\boldsymbol{\mathcal{T}}_{\boldsymbol{\theta}} = \frac{\sin(||\underline{\theta}||)}{||\underline{\theta}||} \boldsymbol{I} + \left(1 - \frac{\sin(||\underline{\theta}||)}{||\underline{\theta}||}\right) \underline{u} \otimes \underline{u} + \frac{1}{2} \left(\frac{\sin(||\underline{\theta}||/2)}{||\underline{\theta}||/2}\right)^2 \boldsymbol{\theta} \tag{28}$$

$$\begin{bmatrix} \delta \underline{u}_k \\ \delta \underline{\theta}_k \\ \delta \underline{u}_{k+1} \\ \delta \underline{\theta}_{k+1} \end{bmatrix} = \begin{bmatrix} \boldsymbol{0}_{\mathbf{3x3}} & \boldsymbol{0}_{\mathbf{3x3}} & & \\ \boldsymbol{0}_{\mathbf{3x3}} & \boldsymbol{\mathcal{T}}_{\boldsymbol{\theta}_k}^{-1} & \boldsymbol{0}_{\mathbf{6x6}} & \\ & & \boldsymbol{0}_{\mathbf{3x3}} & \boldsymbol{0}_{\mathbf{3x3}} \\ & \boldsymbol{0}_{\mathbf{6x6}} & \boldsymbol{0}_{\mathbf{3x3}} & \boldsymbol{\mathcal{T}}_{\boldsymbol{\theta}_{k+1}}^{-1} \end{bmatrix} \cdot \begin{bmatrix} \delta \underline{u}_k \\ \delta \underline{\vartheta}_k \\ \delta \underline{u}_{k+1} \\ \delta \underline{\vartheta}_{k+1} \end{bmatrix} = \boldsymbol{H} \begin{bmatrix} \delta \underline{p}_k \\ \delta \underline{p}_{k+1} \end{bmatrix} \tag{29}$$

The full conversion between displacements at the eccentric node and displacements at the degrees of freedom of the element is given by the following relation, which is used as shown to compute loads.

$$\delta \underline{p}_e = \boldsymbol{B}_{\mathbf{e}} \cdot \boldsymbol{H} \cdot \begin{bmatrix} \delta \underline{p}_k \\ \delta \underline{p}_{k+1} \end{bmatrix} \implies \delta \underline{p}_e^T = \begin{bmatrix} \delta \underline{p}_k^T & \delta \underline{p}_{k+1}^T \end{bmatrix} (\boldsymbol{B}_{\mathbf{e}} \cdot \boldsymbol{H})^T \tag{30}$$

$$\implies (\boldsymbol{B}_{\mathbf{e}} \cdot \boldsymbol{H})^T \begin{bmatrix} \underline{\tilde{f}}_e \\ \underline{\tilde{m}}_e \end{bmatrix} = \boldsymbol{H}^T \cdot \boldsymbol{B}_{\mathbf{e}}^T \cdot \begin{bmatrix} \underline{\tilde{f}}_e \\ \underline{\tilde{m}}_e \end{bmatrix} = \begin{bmatrix} \underline{f}_k \\ \underline{m}_k \\ \underline{f}_{k+1} \\ \underline{m}_{k+1} \end{bmatrix} \tag{31}$$

The method of mapping forces from eccentric nodes to the nodes of the structural mesh, according to the expression shown in Eq. (31), has been applied also to convert aerodynamic loads from the aerodynamic grid points to the structural nodes. Centrifugal forces are already calculated at the nodes of the structure and thus are not converted.

The derivative of the applied eccentric forces is calculated by taking the variation of the eccentric load vector:

$$\begin{bmatrix} \delta \underline{f}_k \\ \delta \underline{m}_k \\ \delta \underline{f}_{k+1} \\ \delta \underline{m}_{k+1} \end{bmatrix} = \underbrace{\left(\delta \boldsymbol{H}^{\mathrm{T}}\right) \cdot \boldsymbol{B}_{\mathbf{e}}^{\mathrm{T}} \cdot \begin{bmatrix} \tilde{\underline{f}}_{\mathrm{e}} \\ \tilde{\underline{m}}_{\mathrm{e}} \end{bmatrix}}_{\text{geometric moment stiffness}} + \underbrace{\boldsymbol{H}^{\mathrm{T}} \cdot \left(\delta \boldsymbol{B}_{\mathbf{e}}^{\mathrm{T}}\right) \cdot \begin{bmatrix} \tilde{\underline{f}}_{\mathrm{e}} \\ \tilde{\underline{m}}_{\mathrm{e}} \end{bmatrix}}_{\text{geometric rotation stiffness}} + \underbrace{\boldsymbol{H}^{\mathrm{T}} \cdot \boldsymbol{B}_{\mathbf{e}}^{\mathrm{T}} \cdot \begin{bmatrix} \delta \tilde{\underline{f}}_{\mathrm{e}} \\ \delta \tilde{\underline{m}}_{\mathrm{e}} \end{bmatrix}}_{\text{material stiffness}} = \boldsymbol{K}_{\mathbf{e}} \begin{bmatrix} \delta \underline{p}_k \\ \delta \underline{p}_{k+1} \end{bmatrix} \tag{32}$$

$$\implies \left[\boldsymbol{K}_{\mathbf{h}} + \boldsymbol{K}_{\mathbf{g}} + \boldsymbol{K}_{\mathbf{m}}\right] \begin{bmatrix} \delta \underline{p}_k \\ \delta \underline{p}_{k+1} \end{bmatrix} = \boldsymbol{K}_{\mathbf{e}} \begin{bmatrix} \delta \underline{p}_k \\ \delta \underline{p}_{k+1} \end{bmatrix} \tag{33}$$

where $\boldsymbol{K}_{\mathbf{h}}$ is the geometric moment stiffness matrix, $\boldsymbol{K}_{\mathbf{g}}$ is the geometric rotation stiffness matrix, and $\boldsymbol{K}_{\mathbf{m}}$ is the material stiffness matrix. The complete derivation of the derivative matrix of the eccentric forces has been provided by Werter [12], and thus the full derivation of the eccentric force derivative matrix will not be repeated here for brevity. Nevertheless, the material stiffness has been briefly revisited within this section, as it has been treated differently during the calculation of the aerodynamic stiffness matrix. The geometric moment stiffness and the geometric rotation stiffness are not dependent on the nature of the applied forces, and thus their form remains unchanged from [12].

To calculate the material stiffness, the variation of the applied force must be calculated, as all remaining quantities are already known. This is defined as the derivative of the eccentric forces, multiplied by the variation of the degrees of freedom at the eccentric node.

$$\begin{bmatrix} \delta \tilde{\underline{f}}_{\mathrm{e}} \\ \delta \tilde{\underline{m}}_{\mathrm{e}} \end{bmatrix} = \left(\frac{d}{d \underline{p}_{\mathrm{e}}} \begin{bmatrix} \tilde{\underline{f}}_{\mathrm{e}} \\ \tilde{\underline{m}}_{\mathrm{e}} \end{bmatrix} \right) \cdot \delta \underline{p}_{\mathrm{e}} \tag{34}$$

Substituting Eq. (30) into the above expression yields the following expression for the variation of the eccentric loads. This expression can then be used to determine the material stiffness matrix. This derivation has been used to evaluate the material stiffness matrix for aerodynamic forces, whilst the original derivation that was provided by Werter [12] has been used for the evaluation of the material stiffness matrix for all other externally applied forces.

$$\begin{bmatrix} \delta \tilde{\underline{f}}_{\mathrm{e}} \\ \delta \tilde{\underline{m}}_{\mathrm{e}} \end{bmatrix} = \left(\frac{d}{d \underline{p}_{\mathrm{e}}} \begin{bmatrix} \tilde{\underline{f}}_{\mathrm{e}} \\ \tilde{\underline{m}}_{\mathrm{e}} \end{bmatrix} \right) \cdot \boldsymbol{B}_{\mathbf{e}} \cdot \boldsymbol{H} \cdot \begin{bmatrix} \delta \underline{p}_k \\ \delta \underline{p}_{k+1} \end{bmatrix} \implies \boldsymbol{K}_{\mathbf{m}} = \boldsymbol{H}^{\mathrm{T}} \cdot \boldsymbol{B}_{\mathbf{e}}{}^{\mathrm{T}} \cdot \left(\frac{d}{d \underline{p}_{\mathrm{e}}} \begin{bmatrix} \tilde{\underline{f}}_{\mathrm{e}} \\ \tilde{\underline{m}}_{\mathrm{e}} \end{bmatrix} \right) \cdot \boldsymbol{B}_{\mathbf{e}} \cdot \boldsymbol{H} \tag{35}$$

Using the expression for the derivative of the aerodynamic forces with respect to degrees of freedom of aerodynamic grid points, given by Eq. (7) from Section II.C, the material stiffness matrix for aerodynamic loads is expressed by Eq. (36). Note that the subscript "e" has been replaced by "a" to indicate that the loads being discussed are due to aerodynamic effects:

$$\boldsymbol{K}_{\mathbf{m}} = \boldsymbol{H}^{\mathrm{T}} \cdot \boldsymbol{B}_{\mathbf{a}}{}^{\mathrm{T}} \cdot \begin{bmatrix} \underline{0} & \underline{0} & \underline{0} & \underline{0} & \frac{d}{d\beta} \tilde{\underline{f}}_{\mathrm{a}} & \underline{0} \\ \underline{0} & \underline{0} & \underline{0} & \underline{0} & \frac{d}{d\beta} \tilde{\underline{m}}_{\mathrm{a}} & \underline{0} \end{bmatrix} \cdot \boldsymbol{B}_{\mathbf{a}} \cdot \boldsymbol{H} \tag{36}$$

where $\boldsymbol{B}_{\mathbf{a}}$ is analogous to $\boldsymbol{B}_{\mathbf{e}}$, except corresponding to aerodynamic loads instead of eccentric loads; $\tilde{\underline{f}}_{\mathrm{a}}$ and $\tilde{\underline{m}}_{\mathrm{a}}$ are similarly analogous to $\tilde{\underline{f}}_{\mathrm{e}}$ and $\tilde{\underline{m}}_{\mathrm{e}}$. The geometric moment and rotation stiffness matrices are unchanged from the matrices provided by Werter [11, 12] and thus have not been discussed further.

B. Iterative Scheme for Computing Derivatives of Aerodynamic Loads

To compute derivatives of aerodynamic loads according to the method outlined in Section II.C by solving Eq. (8), the unknown quantities $da/d\beta$ and $da'/d\beta$ must be evaluated iteratively and substituted into Eq. (9) and Eq. (13).

Derivatives of the thrust and torque coefficients with respect to variations in blade twist have been calculated using blade element theory and momentum theory to obtain two sets of expressions that may be iteratively evaluated until convergence. With momentum theory, thrust and torque coefficients are expressed using the axial and tangential induction factors, whereas blade element theory relates the thrust and torque coefficients to the flow angles.

$$\frac{dC_t}{d\beta} = \frac{\partial C_t}{\partial a}\frac{\partial a}{\partial \beta} + \frac{\partial C_t}{\partial a'}\frac{\partial a'}{\partial \beta} = \frac{dC_t}{d\alpha}\frac{d\alpha}{d\beta} \tag{37}$$

$$\frac{dC_q}{d\beta} = \frac{\partial C_q}{\partial a}\frac{\partial a}{\partial \beta} + \frac{\partial C_q}{\partial a'}\frac{\partial a'}{\partial \beta} = \frac{dC_q}{d\alpha}\frac{d\alpha}{d\beta} \tag{38}$$

Using momentum theory, derivatives of the thrust and torque coefficients with respect to variations in the blade twist angle are given by Eq. (39) and Eq. (40), maintaining all the assumptions discussed in Section II.B:

$$\frac{dC_t^{\mathrm{M}}}{d\beta} = \begin{cases} 4\left(\left(1+2a\right)F + a\left(1+a\right)\frac{\partial F}{\partial a}\right)\frac{da}{d\beta} & a \geq -0.326 \\ \left(1.39F + \left(1.39\left(1+a\right) - 1.816\right)\frac{\partial F}{\partial a}\right)\frac{da}{d\beta} & a < -0.326 \end{cases} \tag{39}$$

$$\frac{dC_q^{\mathrm{M}}}{d\beta} = 4\left(1+a\right)\frac{nr}{V_\infty}\left(F + a'\frac{\partial F}{\partial a'}\right)\frac{da'}{d\beta} + 4a'\frac{nr}{V_\infty}\left(F + \left(1+a\right)\frac{\partial F}{\partial a}\right)\frac{da}{d\beta} \tag{40}$$

where the superscript "M" denotes that C_t^{M} and C_q^{M} are respectively the sectional thrust and torque coefficients computed using momentum theory, and where F is the Prandtl root- and tip-loss factor.

Differentiating the root- and tip-loss factors, F_{root} and F_{tip}, with respect to the incoming flow angle, φ, yields Eq. (41) and Eq. (42), which were derived by directly differentiating expressions for the root and tip loss factors:

$$F_{\mathrm{root}} = \left(\frac{2}{\pi}\right)\cos^{-1}\left(e^{\frac{-N_{\mathrm{b}}}{2}\left(\frac{r-r_{\mathrm{root}}}{r_{\mathrm{root}}|\sin(\varphi)|}\right)}\right) \implies \frac{\partial F_{\mathrm{root}}}{\partial \varphi} = \frac{-N_{\mathrm{b}}}{\pi}\left(\frac{r-r_{\mathrm{root}}}{r_{\mathrm{root}}\left|\sin\left(\varphi\right)\right|}\right)\frac{\cos\left(\varphi\right)}{\sin\left(\varphi\right)}\left(\frac{e^{\frac{-N_{\mathrm{b}}}{2}\left(\frac{r-r_{\mathrm{root}}}{r_{\mathrm{root}}|\sin(\varphi)|}\right)}}{\sqrt{1-e^{-N_{\mathrm{b}}\left(\frac{r-r_{\mathrm{root}}}{r_{\mathrm{root}}|\sin(\varphi)|}\right)}}}\right) \tag{41}$$

$$F_{\mathrm{tip}} = \left(\frac{2}{\pi}\right)\cos^{-1}\left(e^{-\frac{N_{\mathrm{b}}}{2}\left(\frac{r_{\mathrm{tip}}-r}{r|\sin(\varphi)|}\right)}\right) \implies \frac{\partial F_{\mathrm{tip}}}{\partial \varphi} = -\frac{N_{\mathrm{b}}}{\pi}\left(\frac{r_{\mathrm{tip}}-r}{r\left|\sin\left(\varphi\right)\right|}\right)\frac{\cos\left(\varphi\right)}{\sin\left(\varphi\right)}\left(\frac{e^{-\frac{N_{\mathrm{b}}}{2}\left(\frac{r_{\mathrm{tip}}-r}{r|\sin(\varphi)|}\right)}}{\sqrt{1-e^{-N_{\mathrm{b}}\left(\frac{r_{\mathrm{tip}}-r}{r|\sin(\varphi)|}\right)}}}\right) \tag{42}$$

where F_{root} and F_{tip} are respectively the root- and tip-loss factors, N_{b} is the number of propeller blades, r_{root} is the radial location of the blade root, and r_{tip} is the radial location of the blade tip.

The derivatives of the Prandtl root- and tip-loss factor, F, with respect to the axial and tangential induction factors, are given by Eq. (43) and Eq. (44), which are found using the chain rule, as $F = F_{\mathrm{root}} \cdot F_{\mathrm{tip}}$:

$$\frac{\partial F}{\partial a} = \left[\frac{\partial F_{\mathrm{root}}}{\partial \varphi}F_{\mathrm{tip}} + F_{\mathrm{root}}\frac{\partial F_{\mathrm{tip}}}{\partial \varphi}\right]\overbrace{\left[\frac{V_\infty}{V_{\mathrm{eff}}}\frac{n\,r}{V_{\mathrm{eff}}}\left(1-a'\right)\right]}^{\partial\varphi/\partial a} \tag{43}$$

$$\frac{\partial F}{\partial a'} = \left[\frac{\partial F_{\mathrm{root}}}{\partial \varphi}F_{\mathrm{tip}} + F_{\mathrm{root}}\frac{\partial F_{\mathrm{tip}}}{\partial \varphi}\right]\underbrace{\left[\frac{V_\infty}{V_{\mathrm{eff}}}\frac{n\,r}{V_{\mathrm{eff}}}\left(1+a\right)\right]}_{\partial\varphi/\partial a'} \tag{44}$$

With these expressions, all terms within Eq. (39) and Eq. (40) are known except for $da/d\beta$ and $da'/d\beta$. Derivatives of the thrust and torque coefficients with respect to variations in the blade twist may also be evaluated using blade element theory to isolate for derivatives of the angle of attack, computed using either the thrust or torque coefficient expressions, denoted respectively with the subscripts t or q, as shown below. This yields three expressions for $d\alpha/d\beta$:

$$\frac{dC_t^{\mathrm{BE}}}{d\beta} = C_{z_\alpha}\,\sigma\left(r\right)\left(\frac{V_{\mathrm{eff}}}{V_\infty}\right)^2\frac{d\alpha}{d\beta} \implies \left(\frac{d\alpha}{d\beta}\right)_t = \begin{cases} \frac{4\left(\left(1+2a\right)F + a\left(1+a\right)\frac{\partial F}{\partial a}\right)\frac{da}{d\beta}}{C_{z_\alpha}\,\sigma(r)}\left(\frac{V_\infty}{V_{\mathrm{eff}}}\right)^2 & a \geq -0.326 \\ \frac{\left(1.39F + \left(1.39\left(1+a\right) - 1.816\right)\frac{\partial F}{\partial a}\right)\frac{da}{d\beta}}{C_{z_\alpha}\,\sigma(r)}\left(\frac{V_\infty}{V_{\mathrm{eff}}}\right)^2 & a < -0.326 \end{cases} \tag{45}$$

$$\frac{dC_q^{\mathrm{BE}}}{d\beta} = C_{x_\alpha}\,\sigma\left(r\right)\left(\frac{V_{\mathrm{eff}}}{V_\infty}\right)^2\frac{d\alpha}{d\beta} \implies \left(\frac{d\alpha}{d\beta}\right)_q = \frac{4nrV_\infty\left[\left(1+a\right)\left(F + a'\frac{\partial F}{\partial a'}\right)\frac{da'}{d\beta} + a'\left(F + \left(1+a\right)\frac{\partial F}{\partial a}\right)\frac{da}{d\beta}\right]}{C_{x_\alpha}\,\sigma\left(r\right)V_{\mathrm{eff}}^2} \tag{46}$$

where the superscript "BE" denotes that C_t^{BE} and C_q^{BE} are respectively the sectional thrust and torque coefficients computed using blade element theory, and where $\sigma = N_\mathrm{b} c/(2\pi r)$ is the propeller's local solidity.

With three expressions and three unknowns, the derivatives $da/d\beta$ and $da'/d\beta$, may be iteratively solved for using Newton's method by constructing a residual vector, as shown below, and evaluating the system of equations shown in Eq. (48) (presented at the i^{th} iteration) until convergence. After solving for both $da/d\beta$ and $da'/d\beta$, $d\alpha/d\beta$ can be evaluated by substituting these terms into either Eq. (13), Eq. (45), or Eq. (46). All three of these equations will yield the same result. With this, all terms required to evaluate Eq. (8) are known:

$$\underline{R} = \begin{bmatrix} \left(\frac{d\alpha}{d\beta}\right)_t - \frac{d\alpha}{d\beta} & \left(\frac{d\alpha}{d\beta}\right)_q - \frac{d\alpha}{d\beta} \end{bmatrix}^T := \underline{0} \tag{47}$$

$$\begin{bmatrix} \frac{da}{d\beta} \\ \frac{da'}{d\beta} \end{bmatrix}_{i+1} = \begin{bmatrix} \frac{da}{d\beta} \\ \frac{da'}{d\beta} \end{bmatrix}_i - \begin{bmatrix} \frac{\partial R_1}{\partial(da/d\beta)} & \frac{\partial R_1}{\partial(da'/d\beta)} \\ \frac{\partial R_2}{\partial(da/d\beta)} & \frac{\partial R_2}{\partial(da'/d\beta)} \end{bmatrix}_i^{-1} \cdot \underline{R} \tag{48}$$

where $\underline{R}$ is the residual vector that is minimized using Newton's method.

C. TUD-XPROP-3 Blade Geometry and Material Properties

Material Data

Table 3 contains a summary of the materials used in Section III and Section IV (see Table 1). Only unidirectional carbon fibres have been considered for the design of propeller blades because they exhibit a good combination of strength and stiffness [43]. Aluminium was used to model the cantilever box beam during verification of the structural analysis routine in Section III.A. The subscript "11" denotes quantities acting parallel to the plies, while quantities acting orthogonal to the plies are denoted by the subscript "22". The ultimate tensile strength is denoted by the superscript "UT", the ultimate compressive strength is denoted by the superscript "UC", and the shear strength is denoted by τ_{12}^{U}.

Table 3 Material properties used in Section III and Section IV [43, 44].

Material[a,b]	ρ_S	E_{11}	E_{22}	G_{12}	ν_{12}	$\sigma_{11}^{\mathrm{UT}}$	$\sigma_{11}^{\mathrm{UC}}$	$\sigma_{22}^{\mathrm{UT}}$	$\sigma_{22}^{\mathrm{UC}}$	τ_{12}^{U}
AS4 / APC2	1.57	134	8.70	5.1	0.28	2060	1100	78	196	157
Al 6061-T6	2.75	72	72	26.9	0.33	310	310	310	310	207

[a] SI units are used for all dimensional quantities, with g/cm^3 for densities (ρ), GPa for elastic constants (E, G), and MPa for strengths (σ, τ).
[b] Fibre composite materials are conventionally named as follows: "fibre material" / "resin composition".

TUD-XPROP Geometry

Geometry data for the XPROP or XPROP-3 propeller are shown in Fig. 20, and photographs of the two propellers under consideration are provided in [41]. The blade pitch setting is always defined as the twist angle at the 70% span position. Thus, the twist distribution that is shown in Fig. 20b corresponds to a blade pitch setting of approximately 0°.

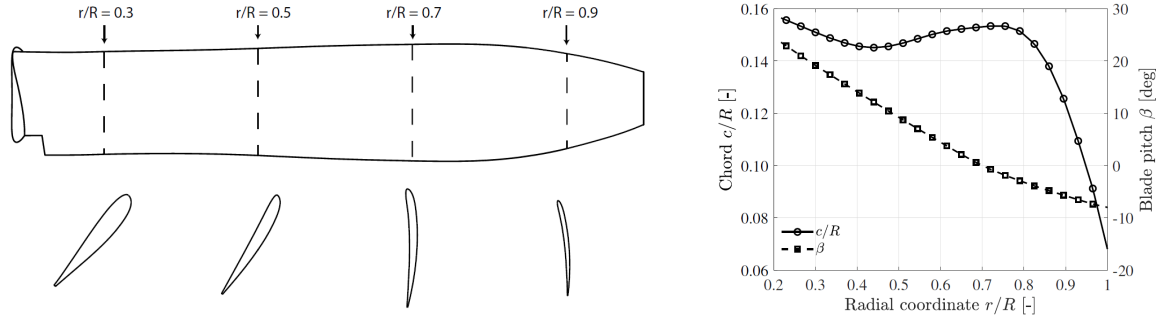

(a) Airfoils at varying spanwise locations.

(b) Chord and twist distributions.

Fig. 20 Geometric data for the TUD-XPROP propeller [20].

Blade geometry data for the TUD-XPROP propeller are provided in [20]. There are two composite propellers with the same blade geometry and either three or six blades (XPROP-3 and XPROP, respectively). The incidence angle of the blades can be manually adjusted, and the diameter of the propeller is 406.4 millimetres. The propeller represents a typical previous-generation turboprop propeller. It has negligible sweep and lean, making its geometry relatively simple, and the two rotors under consideration have been used extensively already for investigations into isolated propeller aerodynamics, propeller integration studies, and distributed propeller studies (i.e. [17, 19, 20]).

D. Stiffness Rosette Plots Supporting Design Sensitivity Studies

Laminate stiffness rosettes have been shown at selected ply orientations, representing symmetric-unbalanced and symmetric-balanced laminates. Only six ply orientations of each type are shown. The in-plane stiffness represents the ability of the laminate to resist in-plane forces, whereas the out-of-plane stiffness represents the ability of the laminate to resist out-of-plane forces. As expected from the stiffness rosettes for symmetric-unbalanced laminates, shown in Fig. 21a for in-plane stiffness and in Fig. 21c for out-of-plane stiffness, the direction of maximum stiffness is closely aligned with the angle that most of the plies are aligned with. This is immediately clear for laminates with $\Theta \in \{-45°, +45°\}$. Laminates with ply orientations of $\pm 30°$ and $\pm 60°$ have slightly skewed stiffness rosettes due to the constant presence of fibres with orientations of 0° and 90°. For symmetric-balanced laminates, Fig. 21b indicates that laminates corresponding to orientations of $(+\Theta, -\Theta)$ and $(-\Theta, +\Theta)$ have equal in-plane stiffness. The out-of-plane stiffness, shown in Fig. 21d, is skewed between laminates with equivalent ply angles of opposite sign, showing more stiffness towards the outermost plies. The difference observed between the out-of-plane stiffness corresponding to ply orientations of $(+\Theta, -\Theta)$ and $(-\Theta, +\Theta)$ would likely be greater if the laminates only consisted of fibres with these corresponding orientations, instead of also containing plies with constant angles of 0° and 90°. For symmetric-balanced laminates, the maximum stiffness is either aligned closely with 0° or 90°, depending on whether $\pm\Theta$ is closer to 0° or 90°, except for at $\Theta = \pm 45°$, where the maximum stiffness is split evenly between the angles +45° and −45°. Without the outermost and innermost fibres that have constant angles of 0° and 90°, the primary stiffness axes of the symmetric-balanced laminates would instead be more closely aligned with the angles given by $\pm\Theta$.

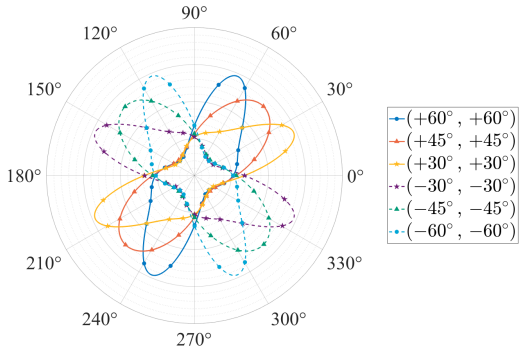

(a) In-plane stiffness (symmetric-unbalanced).

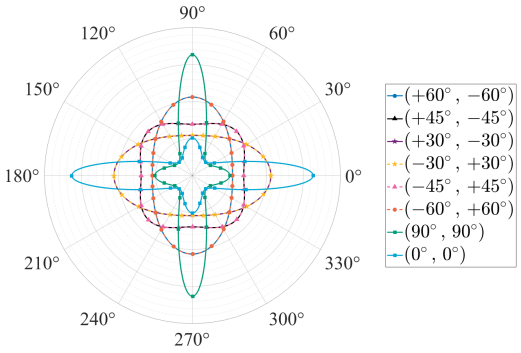

(b) In-plane stiffness (symmetric-balanced).

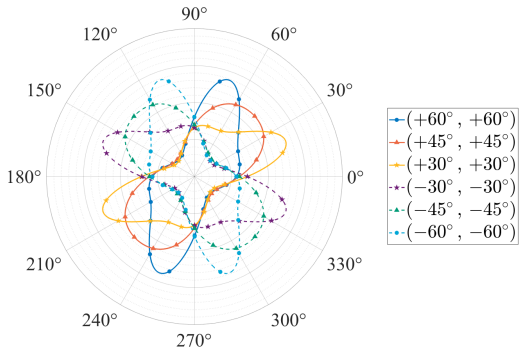

(c) Out-of-plane stiffness (symmetric-unbalanced).

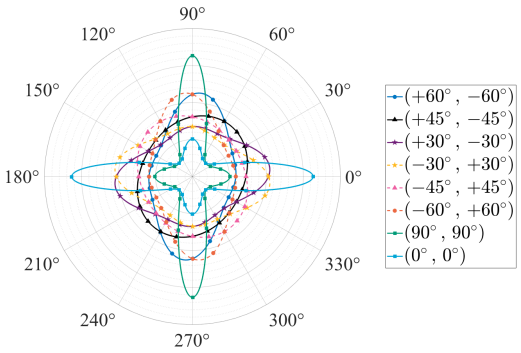

(d) Out-of-plane stiffness (symmetric-balanced).

Fig. 21 Plots of stiffness rosettes for ply orientations considered during sensitivity studies.

References

[1] Dwyer, W. J., and Rogers, J. B., "Aeroelastically Tailored Propellers," SAE Technical Paper 770455, SAE International, 1977. https://doi.org/10.4271/770455.

[2] Yamamoto, O., and August, R., "Structural and Aerodynamic Analysis of a Large Scale Advanced Propeller Blade," *Journal of Propulsion and Power*, Vol. 8, No. 2, 1992, pp. 367–373. https://doi.org/10.2514/3.23487, publisher: American Institute of Aeronautics and Astronautics.

[3] Khan, A. M., "Flexible composite propeller design using constrained optimization techniques," Ph.D. thesis, Iowa State University, 1997. URL https://dr.lib.iastate.edu/handle/20.500.12876/64733.

[4] Khan, A. M., Dayal, V., Vogel, J. M., and Adams, D. O., "Effects of Bend–Twist Coupling on Composite Propeller Performance," *Mechanics of Composite Materials and Structures*, Vol. 7, No. 4, 2000, pp. 383–401. https://doi.org/10.1080/10759410050201717.

[5] Sandak, Y., and Rosen, A., "Aeroelastically adaptive propeller using blades' root flexibility," *The Aeronautical Journal*, Vol. 108, 2004, pp. 411–418. https://doi.org/10.1017/S0001924000000221.

[6] Sodja, J., Drazumeric, R., Kosel, T., and Marzocca, P., "Design of Flexible Propellers with Optimized Load-Distribution Characteristics," *Journal of Aircraft*, Vol. 51, No. 1, 2014, pp. 117–128. https://doi.org/10.2514/1.C032131, publisher: American Institute of Aeronautics and Astronautics.

[7] Möhren, F., Bergmann, O., Janser, F., and Braun, C., "On the influence of elasticity on propeller performance: a parametric study," *CEAS Aeronautical Journal*, 2023. https://doi.org/10.1007/s13272-023-00649-y, URL https://link.springer.com/10.1007/s13272-023-00649-y.

[8] Ferede, E. A., "Static Aeroelastic Optimization of Composite Wind Turbine Blades Using Variable Stiffness Laminates: Exploring Twist Coupled Composite Blades in Stall Control," Ph.D. thesis, Delft University of Technology, 2016. https://doi.org/10.4233/uuid:b4fe0ca4-b8c7-4e23-a2f1-247ac3b61aeb.

[9] Hegberg, T., "Fast Aeroelastic Analysis and Optimisation of Large Mixed Materials Wind Turbine Blades," Ph.D. thesis, Delft University of Technology, 2019. https://doi.org/10.4233/uuid:643ddf12-97d3-48a1-9742-b4dd22f16164.

[10] Gur, O., and Rosen, A., "Optimization of Propeller Based Propulsion System," *Journal of Aircraft*, Vol. 46, 2009, pp. 95–106. https://doi.org/10.2514/1.36055.

[11] Werter, N. P. M., and De Breuker, R., "A novel dynamic aeroelastic framework for aeroelastic tailoring and structural optimisation," *Composite Structures*, Vol. 158, 2016, pp. 369–386. https://doi.org/10.1016/j.compstruct.2016.09.044.

[12] Werter, N. P. M., "Aeroelastic Modelling and Design of Aeroelastically Tailored and Morphing Wings," Ph.D. thesis, Delft University of Technology, 2017. https://doi.org/10.4233/uuid:74925f40-1efc-469f-88ee-e871c720047e.

[13] Rajpal, D., De Breuker, R., Timmermans, H., Lammen, W., and Torrigiani, F., "Including aeroelastic tailoring in the conceptual design process of a composite strut braced wing," *Proceedings of the 31st Congress of the International Council of the Aeronautical Sciences*, 2018. URL http://resolver.tudelft.nl/uuid:5c9b55f4-b3b7-4baf-bd38-f143595d7341.

[14] Ferede, E. A., Abdalla, M. M., Gandhi, F., van Bussel, G., and Dillinger, J. (eds.), *Aeroelastic Optimization of Composite Wind Turbine Blades Using Variable Stiffness Laminates*, Vol. 73, AHS International, 2017. ISSN: 1552-2938.

[15] Ferede, E. A., and Abdalla, M. M. (eds.), *Cross-sectional modelling of thin-walled composite beams*, 2014. https://doi.org/10.2514/6.2014-0163.

[16] Hodges, D. H., *Nonlinear Composite Beam Theory*, American Institute of Aeronautics and Astronautics, 2006. https://doi.org/10.2514/4.866821.

[17] Sinnige, T., Stokkermans, T., van Arnhem, N., and Veldhuis, L. L. (eds.), *Aerodynamic Performance of a Wingtip-Mounted Tractor Propeller Configuration in Windmilling and Energy-Harvesting Conditions*, AIAA Aviation Forum, American Institute of Aeronautics and Astronautics, 2019. URL https://arc.aiaa.org/doi/10.2514/6.2019-3033.

[18] Erzen, D., Andrejasic, M., and Kosel, T. (eds.), *An Optimal Propeller Design for In-Flight Power Recuperation on an Electric Aircraft*, American Institute of Aeronautics and Astronautics, 2018. URL https://arc.aiaa.org/doi/abs/10.2514/6.2018-3206.

[19] Goyal, J., Sinnige, T., Avallone, F., and Ferreira, C., "Aerodynamic and Aeroacoustic Characteristics of an Isolated Propeller at Positive and Negative Thrust," *AIAA Aviation 2021 Forum*, AIAA Aviation Forum, American Institute of Aeronautics and Astronautics, 2021, pp. 1–22. URL https://arc.aiaa.org/doi/abs/10.2514/6.2021-2187.

[20] Nederlof, R., Ragni, D., and Sinnige, T. (eds.), *Experimental Investigation of the Aerodynamic Performance of a Propeller at Positive and Negative Thrust and Power*, AIAA Aviation Forum, American Institute of Aeronautics and Astronautics, 2022. URL https://arc.aiaa.org/doi/abs/10.2514/6.2022-3893.

[21] Binder, N., Courty-Audren, S.-K., Duplaa, S., Dufour, G., and Carbonneau, X., "Theoretical Analysis of the Aerodynamics of Low-Speed Fans in Free and Load-Controlled Windmilling Operation," *Journal of Turbomachinery*, Vol. 137, No. 10, 2015. https://doi.org/10.1115/1.4030308.

[22] Sodja, J., De Breuker, R., Nozak, D., Drazumeric, R., and Marzocca, P., "Assessment of low-fidelity fluid–structure interaction model for flexible propeller blades," *Aerospace Science and Technology*, Vol. 78, 2018, pp. 71–88. https://doi.org/10.1016/j.ast.2018.03.044.

[23] Tsai, S. W., and Hahn, H. T., *Introduction to Composite Materials*, 1st ed., CRC Press, 1980. https://doi.org/10.1201/9780203750148.

[24] Battini, J.-M., and Pacoste, C., "Co-rotational beam elements with warping effects in instability problems," *Computer Methods in Applied Mechanics and Engineering*, Vol. 191, 2002, pp. 1755–1789. https://doi.org/10.1016/S0045-7825(01)00352-8, URL https://doi.org/10.1016/S0045-7825(01)00352-8.

[25] de Breuker, R., "Energy-based Aeroelastic Analysis and Optimisation of Morphing Wings," Ph.D. thesis, Delft University of Technology, 2011. URL http://resolver.tudelft.nl/uuid:867c84ae-6cf5-45aa-ba5f-ab6ec4bbf5ed.

[26] Wald, Q. R., "The aerodynamics of propellers," *Progress in Aerospace Sciences*, Vol. 42, No. 2, 2006, pp. 85–128. https://doi.org/10.1016/j.paerosci.2006.04.001.

[27] Gur, O., and Rosen, A., "Comparison Between Blade-Element Models of Propellers," *The Aeronautical Journal*, Vol. 112, No. 1138, 2008, pp. 689–704. https://doi.org/10.13140/RG.2.1.3854.5129.

[28] Leishman, J. G., *Principles of Helicopter Aerodynamics*, Cambridge University Press, 2006.

[29] Ning, A., "Using blade element momentum methods with gradient-based design optimization," *Structural and Multidisciplinary Optimization*, Vol. 64, 2021, pp. 991–1014. https://doi.org/10.1007/s00158-021-02883-6.

[30] Drela, M., "QPROP Formulation," Tech. rep., Massachusetts Institute of Technology, 2006.

[31] Hepperle, M., "Inverse aerodynamic design procedure for propellers having a prescribed chord-length distribution," *Journal of Aircraft*, Vol. 47, 2010, pp. 1867–1872. https://doi.org/10.2514/1.46535.

[32] Morgado, J. P. S., "Development of an Open Source Software Tool for Propeller Design in the MAAT Project," Ph.D. thesis, University of Beira Interior, 2016. URL http://hdl.handle.net/10400.6/4184.

[33] Silvestre, M. A., Morgado, J., and Páscoa, J. C. (eds.), *JBLADE: A propeller design and analysis code*, 2013. https://doi.org/10.2514/6.2013-4220.

[34] Morgado, J., Silvestre, M. A. R., and Páscoa, J. C., "Validation of New Formulations for Propeller Analysis," *Journal of Propulsion and Power*, Vol. 31, No. 1, 2015, pp. 467–477. https://doi.org/10.2514/1.B35240.

[35] Adkins, C. N., and Liebeck, R. H., "Design of Optimum Propellers," *Journal of Propulsion and Power*, Vol. 10, No. 5, 1994, pp. 676–682. https://doi.org/10.2514/3.23779, publisher: American Institute of Aeronautics and Astronautics.

[36] Betz, A., *Introduction to the Theory of Flow Machines*, Pergamon, 1966. https://doi.org/10.1016/C2013-0-05426-6.

[37] Glauert, H., *Airplane Propellers*, Springer Berlin Heidelberg, Berlin, Heidelberg, 1935, Chap. Aerodynamic Theory: A General Review of Progress Under a Grant of the Guggenheim Fund for the Promotion of Aeronautics, pp. 169–360. https://doi.org/10.1007/978-3-642-91487-4_3.

[38] Snel, H., "Sectional Prediction of 3D Effects for Stalled Flow on Rotating Blades and Comparison with Measurements," *1993 European Community Wind Energy Conference Proceedings*, Netherlands Energy Research Foundation ECN, Germany, 1993, pp. 395–399.

[39] Bosschers, J., Montgomerie, B., Brand, A. J., and van Rooij, R. P. J. O. M. (eds.), *Influence of blade rotation on the sectional aerodynamics of rotating blades*, 1996. URL https://dspace-erf.nlr.nl/bitstreams/21a9ac9a-1fe7-4255-af7a-91da7d10439e/download.

[40] Burton, T. L., Jenkins, N., Bossanyi, E., Sharpe, D., and Graham, M., *Wind Energy Handbook*, 3rd ed., Wiley, 2021.

[41] TU Delft: Faculty of Aerospace Engineering, "Propeller Models," https://www.tudelft.nl/lr/organisatie/afdelingen/flow-physics-and-technology/flight-performance-and-propulsion/flight-performance/propeller-aerodynamics/facilities/propeller-models, 2022. accessed on December 23, 2022.

[42] Ibrahimbegovic, A., "On the choice of finite rotation parameters," *Computational Methods in Applied Mechanics and Engineering*, Vol. 149, 1997, pp. 49–71. https://doi.org/10.1016/S0045-7825(97)00059-5, URL https://doi.org/10.1016/S0045-7825(97)00059-5.

[43] Agarwal, B. D., Broutman, L. J., and Chandrashekhara, K., *Analysis and Performance of Fiber Composites*, 4th ed., John Wiley & Sons, 2017.

[44] Daniel, I. M., and Ishai, O., *Engineering Mechanics of Composite Materials*, 2nd ed., Oxford University Press, 2006. https://doi.org/10.2514/4.866821.